




Lead-free all-inorganic halide perovskite quantum dots: review and outlook

Da Eun Lee¹ · Soo Young Kim² · Ho Won Jang¹ 

Received: 29 February 2020 / Revised: 27 April 2020 / Accepted: 12 May 2020 / Published online: 18 June 2020
© The Korean Ceramic Society 2020

Abstract

Halide perovskite is attracting significant attention in optoelectronic because of its unique properties. Lead-free halide perovskites, in particular, have been studied intensively for their nontoxicity. In addition to the attention given to lead-free halide perovskites, the manufacture of these materials on a quantum scale has also received considerable attention due to the quantum confinement effect. This review discusses the current status of lead-free, all-inorganic halide perovskite quantum dots (LFAIHP QDs). First, synthetic methods for producing quantum dots are introduced; then materials are discussed with a focus on tin, bismuth, antimony, copper-based and double perovskite quantum dots. The properties of these materials—such as their physical structure, optical properties, electrical properties, and stability—are discussed. The application of these materials for solar cells, light-emitting diodes, photodetectors, photocatalysts, and memory devices are also examined. Finally, the limitations of LFAIHP QDs, possible methods to overcome them and prospects for these materials in the future are provided.

Keywords Lead-free · Halide perovskite · Quantum dots · Synthesis · Application

1 Introduction

Halide perovskites emerged as promising materials for electronic and optoelectronic devices such as solar cells [1], light emitting diodes (LEDs) [2], sensors [3], memory devices [4–6], photodetectors [7]. This is because halide perovskites demonstrate unique properties such as tunable band gap, facile synthesis, high absorption efficiency, solution processability, flexibility, fast ion migration and long charge carrier diffusion length [8, 9].

The metal halide perovskite has a simple ABX_3 structure, where A is occupied by organic or inorganic material such as $CH_3NH_3^+$ (MA), $CH(NH_2)^{2+}$ (FA) or-, Cs^+ , and B by a divalent metal cation such as Pb^{2+} or Sn^{2+} , and X by a halide anion [10]. The corner-sharing BX_6 octahedra is the basis of the perovskite, and an A cation occupies the voids between

these octahedra. During the nascent stage of the electronic and optoelectronic industries, organic–inorganic hybrid halide perovskites, such as $MAPbI_3$ and $FAPbI_3$, garnered much attention [11, 12]. However, due to the instability of organic materials, the focus has shifted to all inorganic halide perovskites [8, 13]. Until recently, almost all studies focused on $CsPbX_3$, which contains lead. The toxicity of lead raised concerns and limited the inorganic halide perovskites from practical applications [8, 14]. Thus, the research into lead-free all-inorganic halide perovskites (LFAIHP) has become an important undertaking [15].

In addition, there has been an elevated interest in the manufacture of materials at nanoscale, especially quantum dots (QDs) [16]. QDs are nanometer-sized materials that exhibit strong quantum confinement effects. This characteristic is especially advantageous for lighting devices such as lasers, LEDs [17], or photodetectors because a strong quantum confinement suggests a band gap tunability according to size, and reduced defect states [18–20]. Furthermore, the small size allows convenient surface treatment [18–20] and leads to a lower trap density compared with the same material in the bulk or single crystal morphology. Also, it exhibits a narrower band emission which is an important property for optoelectronic devices. The simplicity of the surface treatment can also indicate the improvement of stability. For

✉ Soo Young Kim
sooyoungkim@korea.ac.kr

✉ Ho Won Jang
hwjang@snu.ac.kr

¹ Department of Materials Science and Engineering, Seoul National University, Seoul 08826, Korea

² Department of Materials Science and Engineering, Korea University, Seoul 028410, Korea

example, while $\text{Cs}_2\text{AgBiI}_6$ cannot be produced in its bulk form due to its low thermodynamic stability—it showed a uniform cubic shape in its QD morphology [21, 22]. The study of QDs might be a practical course of action for discovering novel materials. There has been an enormous effort in fabricating halide perovskite (HP) QDs. The aforementioned also applies to LFAIHPs.

Following the trend in this field, there are numerous discussions regarding the LFAIHP QDs. However, it was recently suggested that the first LFAIHP QDs, CsSnX_3 QDs, were—only reported in 2016 [23]. The change in the number of researches clearly showing the trend related to halide perovskites is presented in Fig. 1. Consequently, additional research into this field is required. This review will include the typical synthesis methods for the manufacture of QDs, materials that are currently synthesized, the devices made with LFAIHP QDs, prospective applications, and finally, a discussion on how to overcome the challenges and prospects of LFAIHP QDs.

2 Synthesis method of quantum dots

Ever since considerable emphasis was placed on HP QDs in optoelectronic fields, the production of high quality quantum dots became important. Substantial efforts were made to fabricate HP QDs with uniform shape, size, and optical properties by a straightforward and reliable method [16]. Various methods, such as ball-milling [24], template-based method [25, 26], and methods based on liquid phase chemical reaction were established [27–30]. Of the aforementioned methods, employing a liquid phase chemical reaction leads to colloidal QDs is considered the most favorable approach because of its simplicity and possibility of mass production. There are three general synthesizing methods that utilize the liquid phase chemical reaction: hot-injection (HI) method,

ligand-assisted reprecipitation (LARP) method, and ultrasonication-based method. We will focus on these.

2.1 Hot-injection method

The HI method has been used to synthesize multiple quantum dots, from oxide semiconductors to halide perovskites, and is the most commonly used method to synthesize LFAIHP QDs. This method usually consists of two steps. The first step is to create an A-site material precursor and the second step is injecting the previous precursor solution into a solution of ligands, while maintaining the precursors and solvent at a high temperature [31]. The first LFAIHP QDs, which were made of CsSnX_3 (cesium tin halide), were successfully obtained via the HI method by Jellicoe et al. [23]. Apart from the synthesis of the basic structure of the ABX_3 system perovskite quantum dots [23], $\text{A}_2\text{BB}'\text{X}_6$ double perovskite [21, 22], A_2BX_6 vacancy ordered perovskite [32–35], and $\text{A}_3\text{B}_2\text{X}_9$ layered structure perovskite quantum dots [65] are reported by applying the HI method.

In 2018, Zhou et al. [21] synthesized $\text{Cs}_2\text{AgBiBr}_6$ quantum dots. They first created cesium oleate by dissolving Cs_2CO_3 in 1-octadecene (ODE) with oleic acid (OA) under an inert atmosphere. The Cs-precursor solution was then injected into the mixture of BiBr_3 , AgNO_3 , ODE, OA, and HBr at 200 °C under a N_2 atmosphere, thus leading to the immediate formation of $\text{Cs}_2\text{AgBiBr}_6$ (Fig. 2a). QDs were formed in 5 s; therefore, the mixture was cooled in an ice-water bath after 5 s. The resulting QDs had a pure cubic shape and high crystallinity (Fig. 2b).

The morphology of QDs synthesized by the HI method is controlled by three factors: the reaction time of the two precursors, the temperature at which the synthesis occurs, and the ratio of the ligands. The influence of the factors can be verified by the synthesis of Cs_2SnI_6 . The first Cs_2SnI_6 QDs were synthesized in 2016 by Wang et al. [34]. They demonstrated that reaction time is an important factor in the HI method. When the reaction lasted for less than 1 min, Cs_2SnI_6 QDs were formed. However, as the reaction time progressed, different shapes of Cs_2SnI_6 nanocrystals were formed. Specifically, 5, 10, 30, and 60 min of reaction time produced nanorods, nanowires, nanobelts, and nanoplatelets, respectively (Fig. 2c). Dolzhenkov et al. [35] confirmed that the reaction temperature plays a crucial role in the size of nanocrystals. As the reaction temperature increased from 80 to 220 °C, the size of the Cs_2SnI_6 nanocrystals became larger (Fig. 2d). Xu et al. [33] reported that different ratios of ligands resulted in different morphologies of the Cs_2SnI_6 nanocrystals. When the two precursors were mixed with oleic acid (OA) exclusively as the ligand, Cs_2SnI_6 QDs with 10 nm diameters were formed. However, as the ratio of OA to octylamine increased to 5:2, 2D nanoplates were formed.

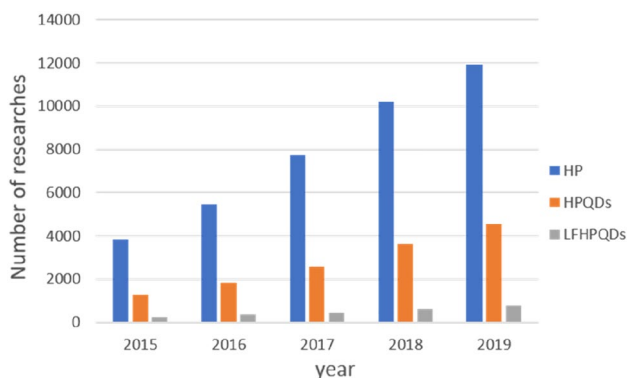


Fig. 1 The number of researches conducted from 2015 to 2019, corresponding to halide perovskites (blue), halide perovskite quantum dots (orange), and lead-free halide perovskite quantum dots (gray)

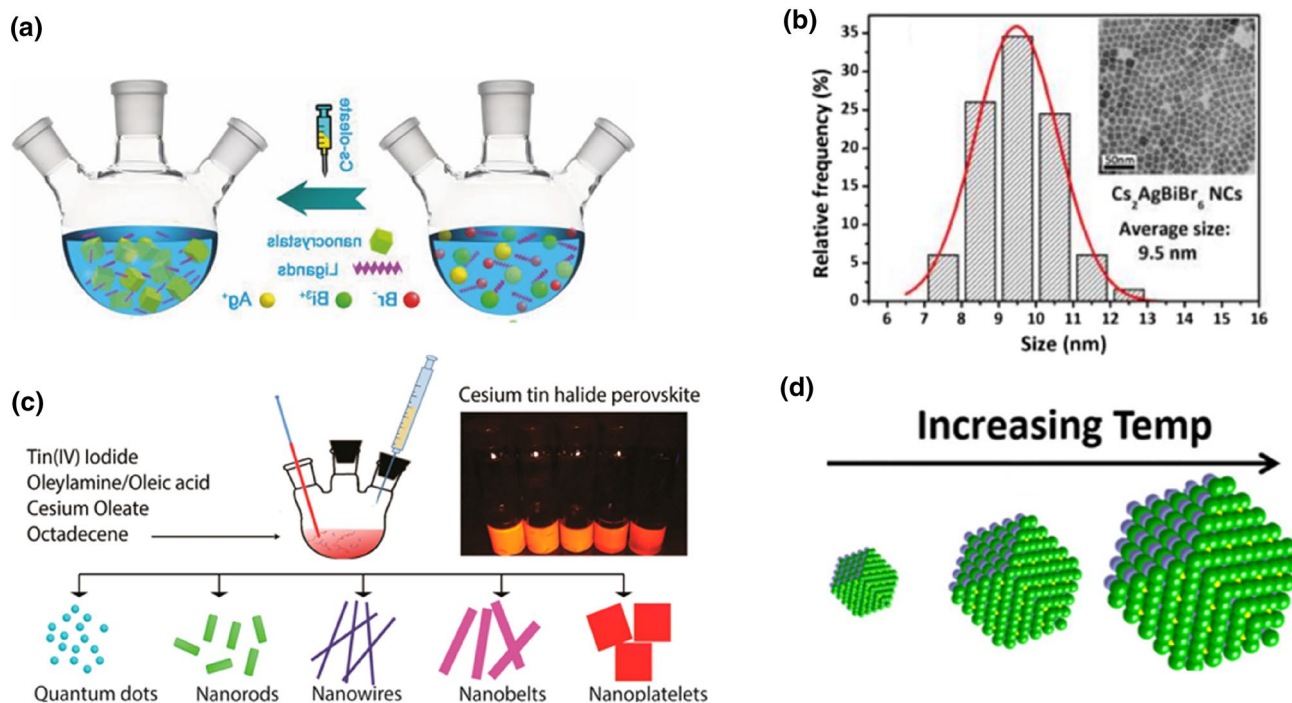


Fig. 2 **a** Schematic illustration of the hot-injection method for the synthesis of $\text{Cs}_2\text{AgBiBr}_6$ QDs. Adapted with permission from Ref. [21]. **b** Size distribution of $\text{Cs}_2\text{AgBiBr}_6$ QDs. The inset is a transmission electron microscopy image of $\text{Cs}_2\text{AgBiBr}_6$ QDs. Adapted with permission from Ref. [21]. **c** Different morphology of Cs_2SnI_6

nanocrystals synthesized by the hot injection method with a difference in the reaction time. Adapted with permission from Ref. [34]. **d** Different size of Cs_2SnI_6 nanocrystals resulting from the synthesizing temperature. Adapted with permission from Ref. [35]

Thus, it is apparent that controlling the ratio of the ligands is an important step in the HI method.

Although the HI method has many advantages, there are many limitations that need to be addressed and resolved. One challenge is that two separate solutions are used during the process and the other is that preheating is required. Two separate precursors are prepared in different flasks at different preheating temperatures. As a result, when the two solutions are mixed, the temperature at which the reaction occurs can vary from the desired temperature; this is particularly true, when the method is applied to large-scale productions. The differences between the two solutions lead to a decline in the reaction temperature and in the inhomogeneous nucleation. Consequently, a one-pot synthesis developed facilitate an enhanced efficiency and reliability. In addition, the desired temperature is usually so elevated that it is not appropriate for commercialization. For example, the required reaction temperature is 170, 220 and 200 °C for CsSnX_3 [23], Cs_2SnI_6 [34], and $\text{Cs}_2\text{AgBiBr}_6$, respectively QDs [21]. Another disadvantage of the HI method is that it typically uses a metal halide as a precursor, which means that the ratio between the B and X ions cannot be controlled. This hinders the possibility of synthesizing materials with a desired stoichiometry. SnI_2 and SnI_4 are used as the precursors of CsSnI_3 [23]

and Cs_2SnI_6 QDs [34]. However, if separate precursors are used as the cation and anion precursors, the two materials can be synthesized through the same process; the only exception will be the modification of the ratio of the precursors. This “three-precursor HI method [21]” will facilitate better control of the ion stoichiometry. In the case of the CsPbX_3 QDs, Yassitepe et al. [36] succeeded in synthesizing CsPbBr_3 QDs of 7–10 nm nanocrystals by employing the “three-precursor HI method”. To achieve the aforementioned synthesis, Cs-acetate and Pb-acetate were used as the metal cation precursors, and quaternary alkylammonium halides-such as tetraoctylammonium halides (TOA-X)-were used as the halide anion precursors. However, these precursors failed to synthesize CsSnI_3 , which indicates that additional research is required concerning the HI method using three precursors. For the LFAIHP QDs, there is only one study that reports using three different sources for synthesizing QDs. Creutz et al. [37] used silver acetate, cesium acetate, and bismuth acetate as the cation precursors and trimethylsilyl halides (TMSX) as the halide anion precursor in the synthesis of $\text{Cs}_2\text{AgBiX}_6$ QDs. The halide precursor solution was injected (at 140 °C) into a solution of metal acetate precursors dissolved in ODE, OA, and OLA, which lead to the immediate nucleation and growth of the QDs (Table 1).

Table 1 Recent reports of lead free all inorganic halide perovskite quantum dots

Material	Methods	Size (nm)	Emission wavelength (nm)	PLQE (%)	Stability	References
CsSnX ₃	HI	10	470–950	0.14	–	[9]
Cs ₂ SnI ₆	HI	2.5	720	0.48	2 weeks in 60% humidity	[34]
Cs ₂ SnI ₆	HI (without ligand)	12	820	–	Stable in air	[35]
Cs ₂ SnI ₆	HI	3	–	–	–	[32]
Cs ₂ SnI ₆	HI	10	701	–	–	[33]
Cs ₂ AgBiBr ₆	HI	9.5	625	–	90 days in air (55% humidity)	[3]
Cs ₂ AgBiX ₆ (X = Br, Cl)	HI	8	646–738	0.3	–	[21]
Cs ₃ Bi ₂ X ₉	LARP	6	400–560	4.5	30 days in air	[43]
Cs ₃ Bi ₂ X ₉	LARP	3.88	393–545	26.4	20% reduction in 78 h illumination	[41]
Cs ₃ Sb ₂ X ₉	LARP	3.07	370–560	46	35 days in air (70% humidity)	[42]
Cs ₃ Bi ₂ I ₉	HI	5	466, 544	1	6 months in ambient air	[61]
Cs ₃ Bi ₂ X ₉	Ultrasonication	9	410–550	0.3	150 days in ambient air	[52]
Cs ₂ AgBiX ₆	HI	8	365–450	–	90 days in air	[22]
Cs ₂ CuX ₄ (X = Br, Cl)	LARP	3.5	388–466	37.5	30 days in air	[44]
Cs ₂ CuCl ₄	HI	6	525	–	–	[67]
Cs ₃ Bi ₂ Br ₉	LARP	3.5	414	22	15% decrease of PL after 180 °C heating	[64]

2.2 Ligand assisted reprecipitation method

Another method for manufacturing colloidal quantum dots is the LARP method [38]. It was suggested to solve the challenges associated with the HI method, i.e., high reaction temperature and low reproducibility when applied to large-scale manufacturing [39]. This is a simple process using the principle of supersaturation in the presence of ligands. The method is widely employed in the synthesis of various QDs and is applicable to the manufacture of LFAIHP QDs. The process initiates by the dropwise transfer of the precursor solution in the polar solvent into a poor solvent containing ligands. The difference in the polarity of the solvents influences the miscibility of the solvents. As a result, the two solvents cannot mix and the precursor encounters a non-equilibrium state. The nucleation and growth of perovskites occur by immediate supersaturation and does not require high temperatures. Room temperature (RT) is sufficient for the synthesis of QDs which indicates that the LARP method can be readily applied to large-scale manufacturing with a high production yield of stable QDs. In 2016, a gram-scale synthesis of lead-based AIHP QDs was reported and used for LED devices [2, 40]. The LARP method is also suitable for LFAIHP QDs [41–44].

Yang et al. [43] synthesized Cs₃Bi₂Br₉ QDs by a one-step reaction without ligands. CsBr and BiBr₃ were dissolved in dimethyl sulfoxide (DMSO) to form a precursor solution. DMSO is a polar solvent; therefore, when the precursor solution is added (dropwise) to the isopropanol—thereby acting as an antisolvent—a yellow–green colloidal solution forms.

This indicates the nucleation and growth of the Cs₃Bi₂Br₉ QDs by reprecipitation. Surprisingly, even in the absence of ligands, it was still possible to yield stable Cs₃Bi₂Br₉ QDs with 6.0 ± 2.2 nm in diameter. However, the low quantum yield of 0.2% indicated the necessity of ligands. In 2018, Leng et al. [41] produced Cs₃Bi₂Br₉ QDs via the LARP method, using OA and oleylamine (OLA) as ligands. The synthetic procedure was similar to previous work [43] except for two conditions. The first difference was that acetone was used as the antisolvent instead of isopropanol; the second was that the precursor solution was prepared with OLA and the antisolvent was prepared with OA (Fig. 3a). The resulting Cs₃Bi₂Br₉ QDs had an average diameter of 3.88 nm (Fig. 3b–d), and a PLQE of 19.4%. The synthesis of the Cs₃Bi₂Br₉ QDs by LARP was conducted by Zhang et al. [42] An average QD size of 3.07 nm was observed whereas the PLQE was as high as 46%. In the procedure, DMSO was used as a polar solvent for the precursor solution and the precursor solution contained OLA or octylamine. Octane, along with the OA ligand was used as an antisolvent.

Although the LARP method is advantageous in terms of the reaction temperature, there are some critical problems to be solved. When the QDs are formed by the HI method, nucleation occurs at a very early stage, followed by growth and stabilization of the size of the QDs, so that isolating the stage between nucleation and growth is possible. However, the nucleation and growth stages cannot be separated with time in the LARP method. Thus, it is difficult to control the size and morphology of QDs [45]. Another

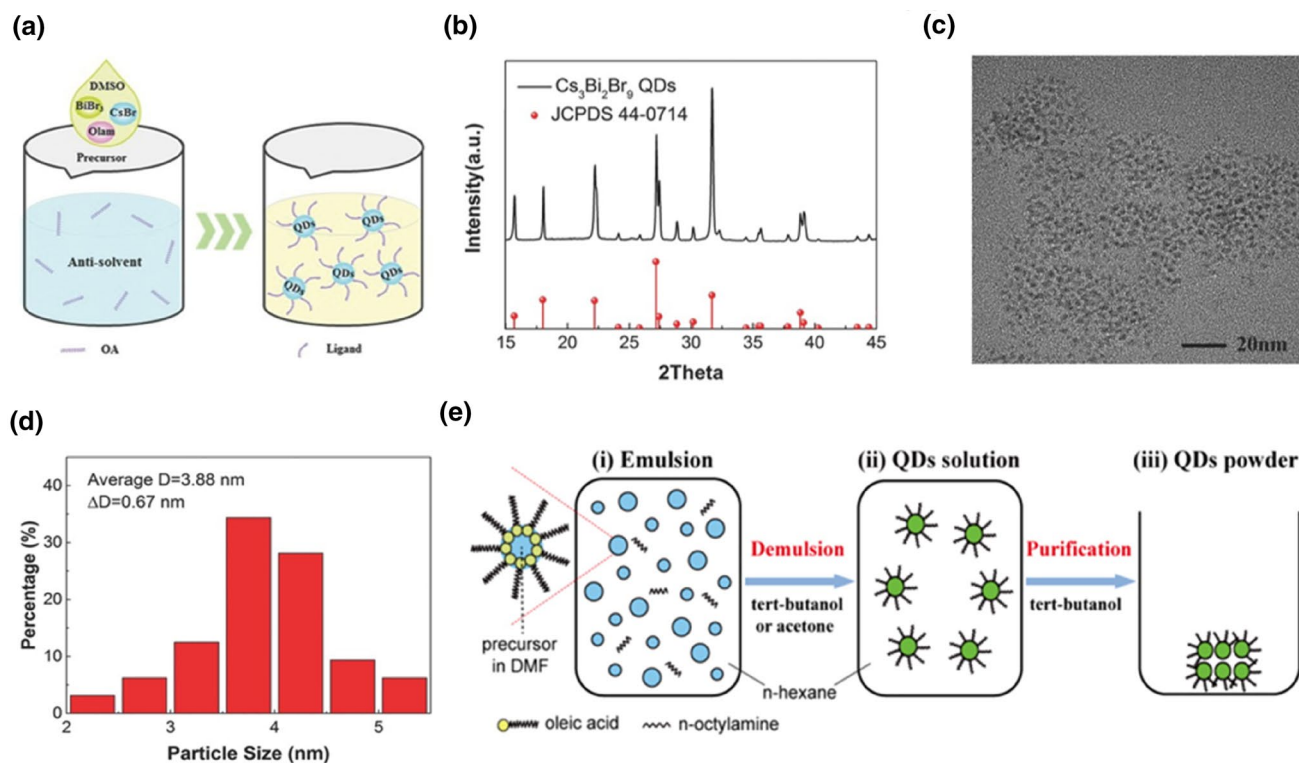


Fig. 3 **a** Schematic illustration of the LARP method for the synthesis of Cs₃Bi₂Br₉ QDs. Adapted with permission from Ref. [41]. **b** X-ray diffraction patterns of the QD powder. Adapted with permission from Ref. [41]. **c** Transmission electron microscopy image of a typical QD. Adapted with permission from Ref. [41]. **d** Analysis of the size distribution.

Adapted with permission from Ref. [41]. **e** Schematic illustration of the QD emulsion LARP method, (i) formation of the emulsion, (ii) demulsification by adding a demulsifier, and redispersion into the colloidal solution, (iii) purification into a solid-state powder. Adapted with permission from Ref. [48]

problem is that the LARP method utilizes a polar solvent during the synthesis. The HP QDs are vulnerable to polar solvents, e.g., DMSO. Therefore, there is a high possibility that the as-synthesized QDs will undergo degradation or encounter the formation of aggregated or poorly crystallized QDs [46, 47]. This effect could be reduced by the “microemulsion LARP method [31]”. Emulsion LARP begins by creating micelles consisting of the precursors, surrounded by ligands using the phenomenon of the self-assembly of ligands in a mixture of polar and non-polar solvents [48–50]. When a demulsifier with a moderate polarity is added, diffusion occurs between the polar and non-polar solvents such that reprecipitation occurs, resulting in the formation QDs (Fig. 3e). However, there has been no evidence reported confirming that the LFAIHP QDs are synthesized by the emulsion LARP method. Yet the fact that Pb-based AIHP QDs are made via this mechanism [51] demonstrates the high potential of the method in terms of its applicability to LFAIHP QDs. Finally, an exploration of the use of the green solvents is required because the polar solvents commonly used in LARP, such as DMF or DMSO, are toxic.

2.3 Ultrasonication method

The ultrasonication method is a direct, one-pot, single-step synthesis process that occurs under a relatively low temperature (typically room temperature) [28] and can be applied to large-scale production [42]. All precursors are mixed in an appropriate solvent with capping ligands such as OA and then sonicated. The successful synthesis of Pb-based AIHP QDs by the ultrasonication method has been reported previously [27–30]. The transmission electron microscopy images of the CsPbX₃ QDs showed that nucleation and growth occur in order, thereby facilitating the separation of the nucleation and growth stages with reaction time [28]. Additionally, this method enables the incorporation of various types of reagents [27, 30]. Based on these results, LFAIHP QDs were synthesized simply by changing the precursor materials [52]. The precursor solution was prepared by dissolving CsI and bismuth acetate in propylene carbonate with OA as the ligand. The mixture was then sonicated at an ultrasound amplitude at room temperature (Fig. 4a), thereby forming uniform and well-dispersed Cs₃Bi₂I₉ QDs with an average size of 9 nm in diameter (Fig. 4b, c) [52].

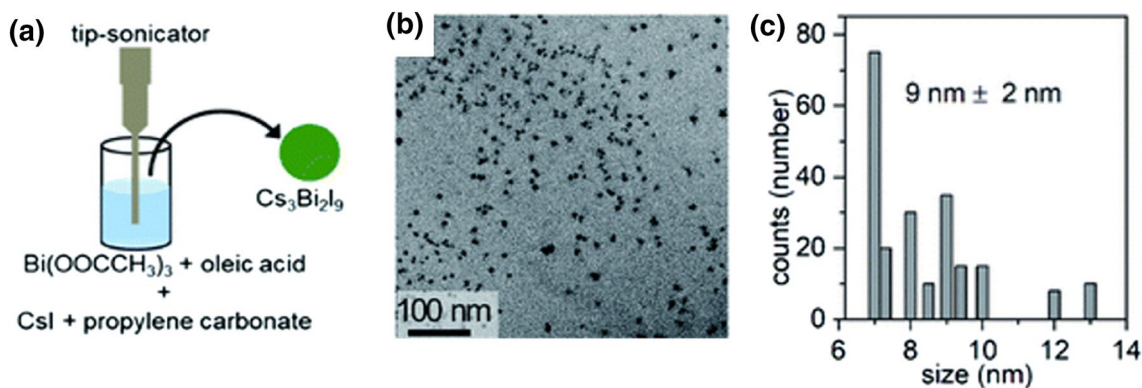


Fig. 4 **a** Schematic illustration of the ultrasonication-based method for the synthesis of $\text{Cs}_3\text{Bi}_2\text{I}_9$ QDs. **b** Transmission electron microscopy image of QDs. **c** Analysis of the distribution of QD sizes. Adapted with permission from Ref. [52]

3 Materials

For the LFAIHP QDs, the A-site is usually occupied by Cs, so that the types of LFAIHP QDs can be divided by a B-site material. The alternative candidates for the B-site, to eliminate the use of Pb, include Sn, Ti, Bi, Sb, Cu, Ag, and In. The structure of the perovskite is determined by the electronic state of the B-site material [38]. Here, we will cover Sn, Bi or Sb, and Cu-based perovskite and double perovskites where two kinds of metals are used alternatively at the B-site.

3.1 Sn-based halide perovskite quantum dots

Tin (Sn) is one of the first materials that was proposed to be used as an alternative for lead (Pb) because of their similar chemical properties. That is, because Sn and Pb both possess s^2 valence electron configuration. However, since Sn has a significantly lower toxicity compared with lead, Sn is considered as a favorable alternative. Furthermore, Sn-based perovskites have a smaller volume change compared to their Pb-based counterparts when structural distortions occur, thus facilitating a small stabilization energy [53]. Figure 5a shows the theoretical structure of CsSnX_3 . The green atom corresponds to the halide anion and the blue atom corresponds to the Cs cation. The gray octahedra is SnX_6 . However, they discovered that the distortion occurred as a consequence of the increased size of the halide ion. Furthermore, while the chloride ions produce a cubic space group (Pm3m), both bromide and iodide form crystal structures of lower symmetry, specifically, orthorhombic (Pnma), which changes to Pm3m when the temperature is increased. This result was consistent with that of previous research performed for the bulk CsSnX_3 [54].

The first Sn-based HP QDs were synthesized in 2016 by Jellicoe et al. [23] who successfully synthesized the CsSnX_3 QDs using the HI method. The Cs precursor was prepared

by dissolving Cs_2CO_3 in 1-octadecene with oleic acid and oleylamine ligands. The SnX_2 solution that was dissolved in tri-*n*-octylphosphine was then swiftly injected into the Cs-precursor at 170 °C, followed by immediate quenching in an ice-water bath. The halide composition ratio could be tuned by varying the halide ratio of the SnX_2 precursor or via the anion-exchange reaction after the pure HP QDs were formed (Fig. 5b). The colloidal CsSnX_3 QDs demonstrate a perfect cubic morphology with an average size of 10 nm in length (Fig. 5c). The PL measurements showed that the optical band gaps of the CsSnX_3 QDs extended from the visible to the near-IR region. By manipulating the halide composition, the optical band gap shifted from 470 nm corresponding to CsSnCl_3 to 950 nm corresponding to CsSnI_3 (Fig. 5d). The measured photoluminescence quantum efficiency (PLQE) of CsSnI_3 was only 0.14% [23]. Considering that the PLQE of the Pb-based AIHP QDs can be more than 90%, this value is too low to be considered an appropriate alternative for traditional perovskite QDs. From the PL decay data of CsSnBr_3 , an interesting phenomenon was observed that synthesizes Sn-based AIHP QDs from Pb-based AIHP QDs [55]. As shown in Fig. 5e, two decay channels were observed: a fast PL decay time of 8.3 ns and a slow PL decay time of 0.7 ns (Fig. 5e). The fast decay in luminescence was attributed to the movement of carriers between the band-edge states, whereas slow decay was on account of the recombination of states just below the band edge. The recombination was possible because the Sn-based perovskites form intrinsic shallow defect sites. The red shift in the PL measurement also supported the existence of shallow defects. The large defect density made a critical difference from the Pb-based AIHP QDs.

CsSnI_3 is the most studied material among the CsSnX_3 . CsSnI_3 has four types of polymorphs, black-alpha, black-beta, black-gamma and yellow phase [56]. The black-gamma polymorphs are the most stable states at RT compared to the alpha and beta polymorphs. Therefore, the

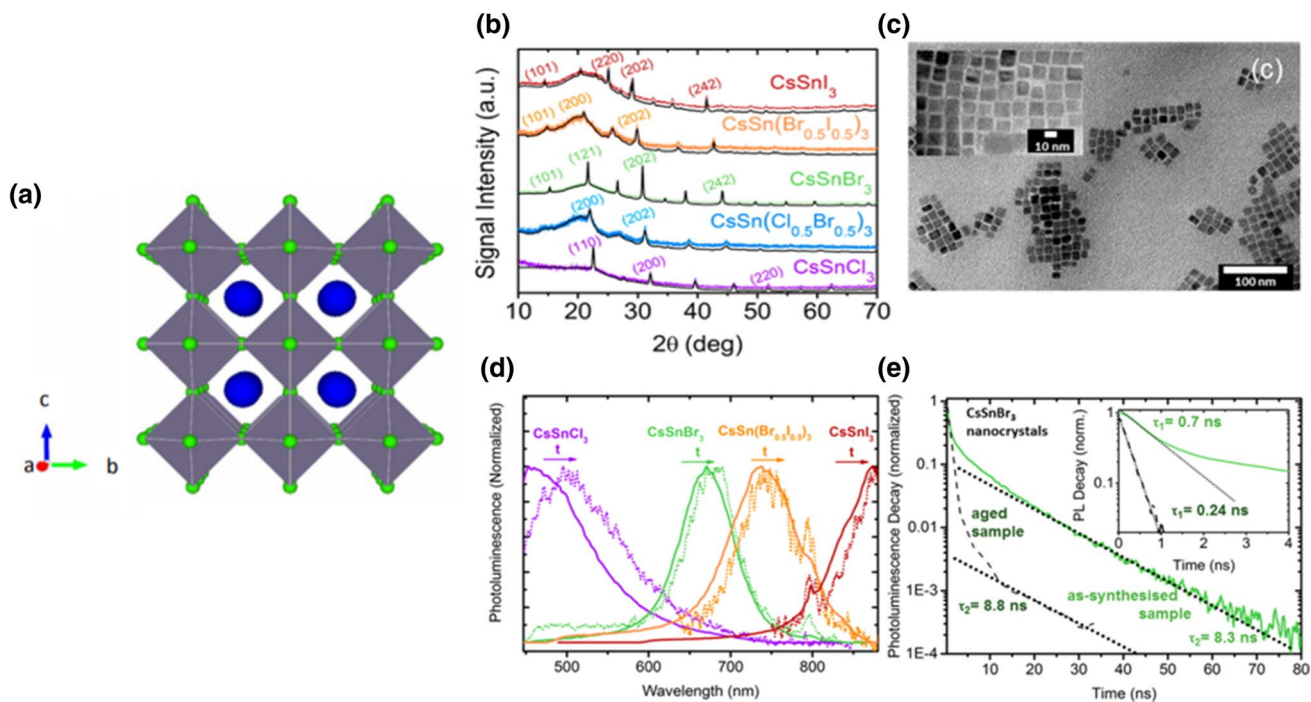


Fig. 5 **a** Structure of the CsSnCl_3 . SnCl_6 octahedra with Cl (green). The Cs atoms (blue) occupy the A sites in the ABX_3 perovskite structure. **b** X-ray diffraction pattern of CsSnX_3 ($X=\text{Cl}$, $\text{Cl}_{0.5}\text{Br}_{0.5}$, Br , $\text{Br}_{0.5}\text{I}_{0.5}$, I) perovskite nanocrystals. **c** Transmission electron microscopy image of the CsSnI_3 nanocrystals. **d** PL of the as-synthesized CsSnX_3 ($X=\text{Cl}$, Br , $\text{Br}_{0.5}\text{I}_{0.5}$, I) perovskite nanocrystals after an ultra-short excitation ($< \text{ps}$) at 400 nm. The colored solid lines indicate the

integrated PL from 0 to 5 ns for each sample. Dashed lines indicate the integrated PL at time-slices of 30–60 ns (CsSnCl_3), 5–8 ns (CsSnBr_3), 30–50 ns ($\text{CsSn}(\text{Br}_{0.5}\text{I}_{0.5})_3$), and 8–30 ns (CsSnI_3). **e** Fast (inset) and slow PL decay kinetics of the as-synthesized and aged CsSnBr_3 nanocrystals in solution, excited at 490 nm, and detected at 590–900 nm. Adapted with permission from Ref. [23]

electrical properties were studied for black-gamma polymorphs. CsSnI_3 is an intrinsic p-type semiconductor with a direct band gap. The reported carrier concentration at RT is $\sim 10^{17} \text{ cm}^{-3}$ and the hole mobility is $\sim 585 \text{ cm}^2\text{V}^{-1} \text{ s}^{-1}$. A high electrical conductivity with a metallic temperature dependence character was observed. Since theoretical calculations showed that the activation energy of the Sn-vacancy is low, this characteristic was attributed to the formation of a Sn-vacancy, which is the main parameter that influences the carrier concentration in the material. It indicates that manipulating the carrier concentration, PL intensity, and electrical property is all possible by controlling the Sn-vacancy in CsSnI_3 [56].

When CsSnI_3 QDs are maintained in ambient air for approximately 5 min, the Sn^{2+} is converted into the more stable Sn^{4+} and the PLQE declines to under 0.01% [23]. This instability of CsSnX_3 in air piqued interest in Cs_2SnX_6 [34]. Tin largely exists as Sn^{4+} , which is its most stable ionic state; therefore, Cs_2SnX_6 possesses characteristics that allows it to be stable in air. As seen in Fig. 6a, this material possesses an anti-fluorite structure, consisting of four $(\text{SnI}_6)^{2-}$ octahedra at the corners and the face centers of the cube and eight Cs^+ cations at the tetragonal interstitials, resulting in a 0D perovskite

structure [32, 34]. This structure is termed a defect-variant perovskite structure. The successful synthesis of Cs_2SnI_6 QDs through the simple HI method has been reported [32–35]. However, to the best of our knowledge, the manufacture of Cs_2SnBr_6 and Cs_2SnCl_6 QDs has not yet been reported. The band gap of the Cs_2SnI_6 QDs with 5 nm diameter was measured to be 1.48 eV (Fig. 6c–e) [34]. The PLQE of the Cs_2SnI_6 QDs was 0.48% which is extremely low [34]. Although the bulk Cs_2SnI_6 is an intrinsic n-type semiconductor, due to the high iodine vacancy, the field effect transistor (FET) made from Cs_2SnI_6 nanobelts showed a p-type conductivity with a high hole mobility of 20.2 cm^2 , which is comparable to the best optimum hole mobility of the organic FETs [34]. The electrical properties of Cs_2SnI_6 QDs have not yet been studied; however, based on the result in which the nanobelts were revealed to have p-type conductivity, we expect that the QDs will similarly show p-type conductivity with a high hole mobility.

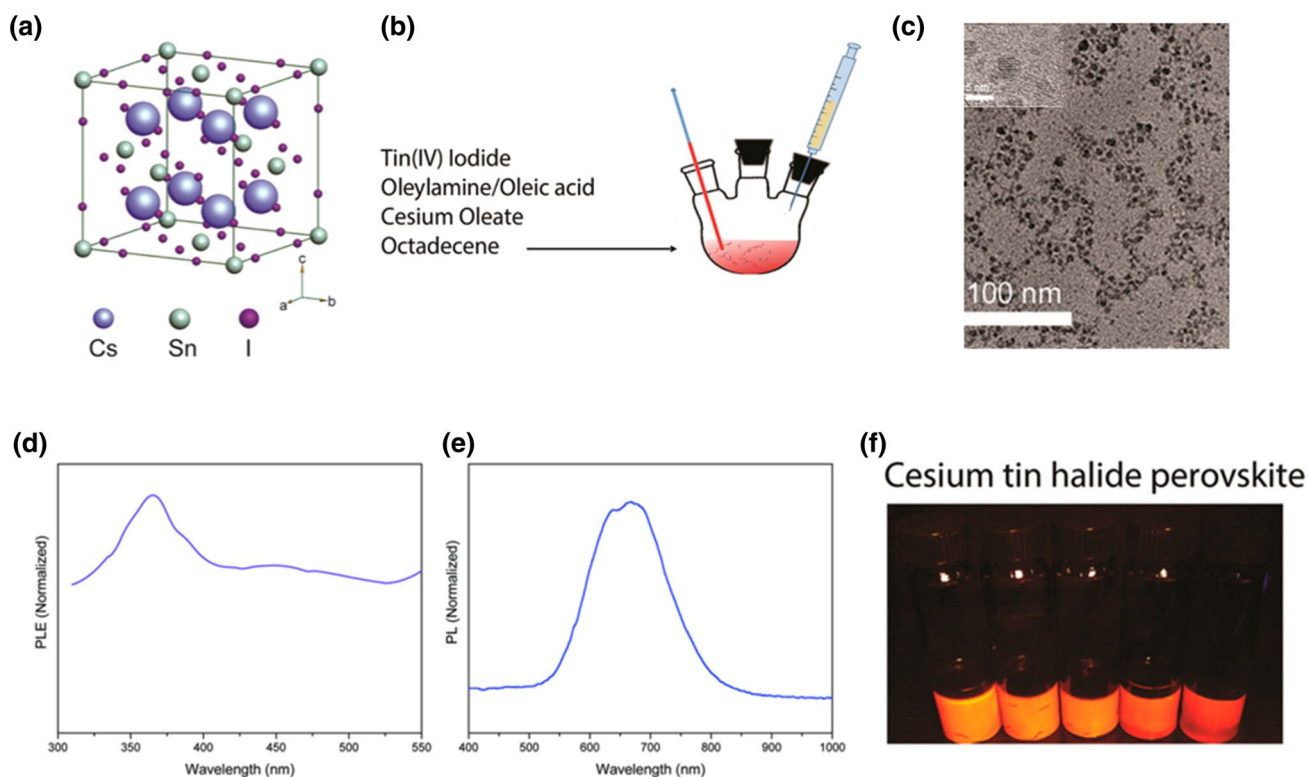


Fig. 6 **a** Crystal structure of Cs_2SnI_6 (cubic, space group $Fm\bar{3}m$, $a = 11.65 \text{ \AA}$), which was obtained by removing half of the Sn atoms at intervals. **b** Schematic of procedures for the controlled synthesis of perovskite Cs_2SnI_6 nanocrystals. **c** Transmission electron microscopy and high-resolution transmission electron microscopy image of

Cs_2SnI_6 spherical quantum dots **(d)** PL emission spectrum of Cs_2SnI_6 spherical quantum dots. **(e)** Excitation spectrum of Cs_2SnI_6 spherical quantum dots. **(f)** Photograph of the as-prepared Cs_2SnI_6 samples under UV light Adapted with permission from Ref. [34]

3.2 Trivalent metal cation (Bi, Sb)-based halide perovskite quantum dots

When the B-site has a trivalent metal cation, the perovskite has an ionic stoichiometry of $\text{A}_3\text{B}_2\text{X}_9$. The most used material is bismuth (Bi), but antimony (Sb) is also used. These elements are considered promising candidates for Pb because they possess ns^2 electronic configuration similar to Pb [57].

$\text{Cs}_3\text{Bi}_2\text{X}_9$ has a similar band structure to CsPbX_3 . This feature arises from the valence band maximum exhibiting antibonding features and the conduction band minimum being stabilized by the spin–orbit splitting between the 6p orbital of bismuth and the 4 or 5-*p* orbital of the halide [58, 59]. The crystal structure is derived from the conventional ABX_3 structure by removing every third $\langle 111 \rangle$ oriented B layer, thus resulting in 2D layered perovskites (Fig. 7a) [42]. Spatial symmetry is determined by the type of halide ion. $\text{Cs}_3\text{Bi}_2\text{I}_9$ and $\text{Cs}_3\text{Bi}_2\text{Br}_9$ have hexagonal $P3m1$ symmetry while $\text{Cs}_3\text{Bi}_2\text{Cl}_9$ has monoclinic $P21/n$ symmetry [60, 61]. The first $\text{Cs}_3\text{Bi}_2\text{X}_9$ QDs are reported by Yang et al. [43] in 2017. They synthesized the QDs by the LARP method and studied the optical properties. Uniform $\text{Cs}_3\text{Bi}_2\text{Br}_9$ QDs with

quasi-spherical shapes and sizes of 6 nm in diameter were synthesized without ligands (Fig. 7b, c). The PL emission peak of the $\text{Cs}_3\text{Bi}_2\text{X}_9$ QDs shifted from 400 to 560 nm, corresponding to the pure $\text{Cs}_3\text{Bi}_2\text{Cl}_9$ QDs and $\text{Cs}_3\text{Bi}_2\text{I}_9$ QDs, respectively (Fig. 7d, e). The PLQE of $\text{Cs}_3\text{Bi}_2\text{Br}_9$ QDs was 0.2%, which could be improved to 4.5% by adding OA during synthesis. The reason for this improvement was assumed to be the reduced surface trap through the passivation of OA. The passivation of OA not only influenced the PLQE but also the stability. The OA capped $\text{Cs}_3\text{Bi}_2\text{Br}_9$ QDs demonstrated superior stability in that it could endure more than 30 days in air. Also, it exhibited good photostability. Specifically, only a 23% decrease in the PL intensity was observed after 400 min of continuous UV illumination [43]. Further increase in the PLQE was observed by the usage of an additional ligand along with OA. From the temperature-dependent PL spectra, it was determined that the radiation of the $\text{Cs}_3\text{Bi}_2\text{Br}_9$ QDs is mainly a consequence of exciton recombination, and not from the radiative recombination of free electrons and holes due to a large exciton binding energy [41]. Additional studies on the time-dependent PL spectra suggested two different path of PL decay. The first is exciton recombination and the second, surface defect

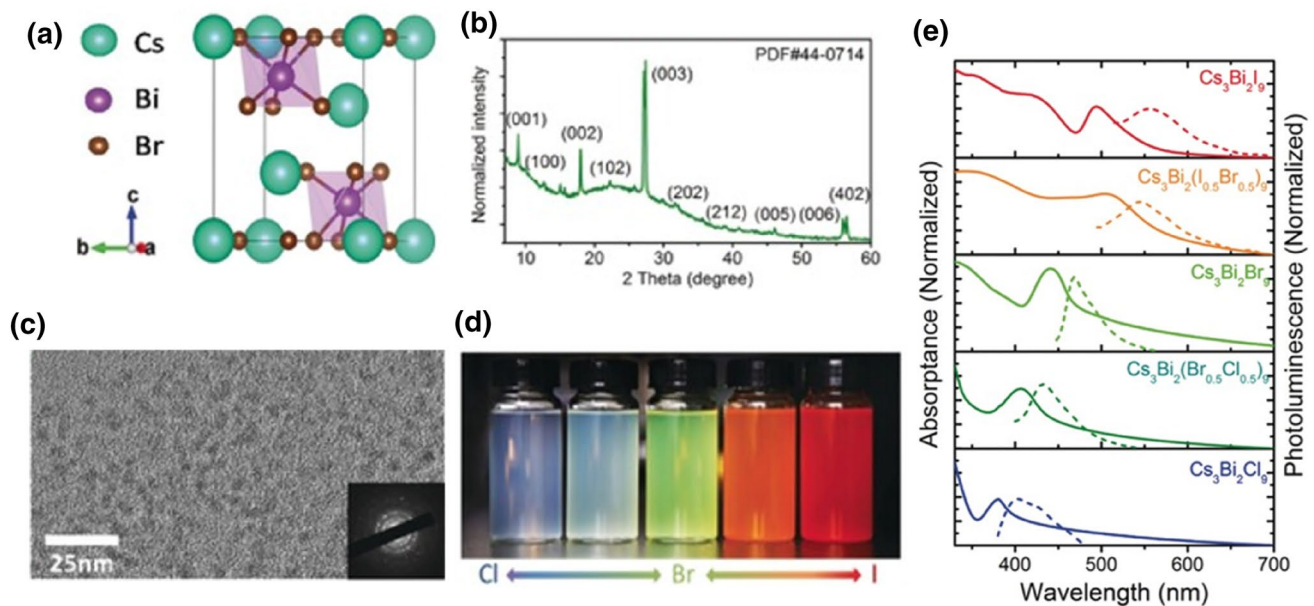


Fig. 7 **a** $\text{Cs}_3\text{Bi}_2\text{Br}_9$ unit cell. **b** X-ray diffraction patterns of $\text{Cs}_3\text{Bi}_2\text{Br}_9$ QDs. **c** Transmission electron microscopy image of $\text{Cs}_3\text{Bi}_2\text{Br}_9$ QDs. **d** Photographs of as-obtained colloidal $\text{Cs}_3\text{Bi}_2\text{X}_9$ ($X = \text{Cl}, \text{Cl}_{0.5}\text{Br}_{0.5}, \text{Br},$

$\text{Br}_{0.5}\text{I}_{0.5}, \text{I}$). **e** Steady-state absorption and PL spectra of QDs containing pure and mixed halides. Adapted with permission from Ref. [43]

recombination [41, 62, 63]. This indicates that surface passivation can decrease the surface defects, subsequently increasing the PLQE. So, more studies on the $\text{Cs}_3\text{Bi}_2\text{X}_9$ QDs were performed with additional ligands. Leng et al. [41] raised the PLQE of the $\text{Cs}_3\text{Bi}_2\text{Br}_9$ QDs up to 26.4% by utilizing OLA along with OA. Lou et al. [64] raised it to 22% by using octylammonium along with OA. In addition to through LARP, the $\text{Cs}_3\text{Bi}_2\text{I}_9$ QDs were also synthesized by the HI method, [65] and the sonication method [52].

Another trivalent metal cation based LFAIHP QDs, $\text{Cs}_3\text{Sb}_2\text{X}_9$ QDs, was reported by Zhang et al. [42] $\text{A}_3\text{Sb}_2\text{X}_9$ exists in a 2D layered form with a good stability similar to that of the Bi perovskites [66]. More specifically, $\text{Cs}_3\text{Sb}_2\text{Br}_9$ consists of bi-octahedral $(\text{Sb}_2\text{Br}_9)^{3-}$ surrounded by cesium cations with a $\text{P}\bar{3}\text{m}1$ space group [42]. The $\text{Cs}_3\text{Sb}_2\text{X}_9$ QDs were synthesized by the LARP method at RT using OA as the ligand. The PL emission peak could be tuned from 370 to 560 nm via anion exchange in a manner analogous to that of $\text{Cs}_3\text{Bi}_2\text{X}_9$ QDs. Among the $\text{Cs}_3\text{Sb}_2\text{X}_9$ QDs, the $\text{Cs}_3\text{Sb}_2\text{Br}_9$ QDs were studied in detail because only bromide QDs were highly luminescent [42]. The $\text{Cs}_3\text{Sb}_2\text{Br}_9$ QDs had a direct band gap of 2.36 eV and the synthesized QDs had an average size of 3.07 nm. The emission peak of the QDs signified a blue shift of 120 nm compared to the single crystal because of strong quantum confinement. The PLQE of these QDs were 46%, and 41 nm full width at half maximum (FWHM), which were superior to all other LFAIHP QDs. This was indicative of the suppression of nonradiative recombination and was attributed to the large exciton binding energy and

quasi-quantum-well band structure arising from the Br-rich surface. The $\text{Cs}_3\text{Sb}_2\text{Br}_9$ QDs also showed superior photo- and air-stability. Under 108 h of sun illumination, only a 28% decrease in the PL intensity was observed and a 50% decrease was observed under 108 h of UV illumination. When stored in air for 35 days, there was a 30% decrease in the PL intensity [42].

3.3 Cu-based halide perovskite quantum dots

As a lead replacement, copper is another promising candidate. Since the divalent ionic state is the most stable state for Cu, the copper-based halide perovskite usually takes the ion stoichiometry of Cs_2CuX_4 which is a 2D perovskite material (Fig. 8a) [44, 67]. The research on this material is limited and requires that significant efforts be made to allow for a comprehensive understanding of the optical and electrical properties before it can be introduced to the market. Yang et al. [44] succeeded in synthesizing Cs_2CuX_4 QDs for the first time in 2018. The XRD data of the Cs_2CuBr_4 and Cs_2CuCl_4 QDs exhibited an orthorhombic crystal structure (Fig. 8b). By modifying the halide composition, the PL emission peak can be finely tuned from 385 nm—which corresponds to pure Cs_2CuCl_4 —to the 504 nm corresponding to $\text{Cs}_2\text{Cu}(\text{Br}/\text{I})_4$ QDs (Fig. 8c). Therefore, the Cs_2CuX_4 QDs exhibits a blue-green luminescence. In addition to changing the halide composition, the emission peak of the Cs_2CuBr_4 QDs could be tuned from 388 to 466 nm by adjusting the precursor ratio

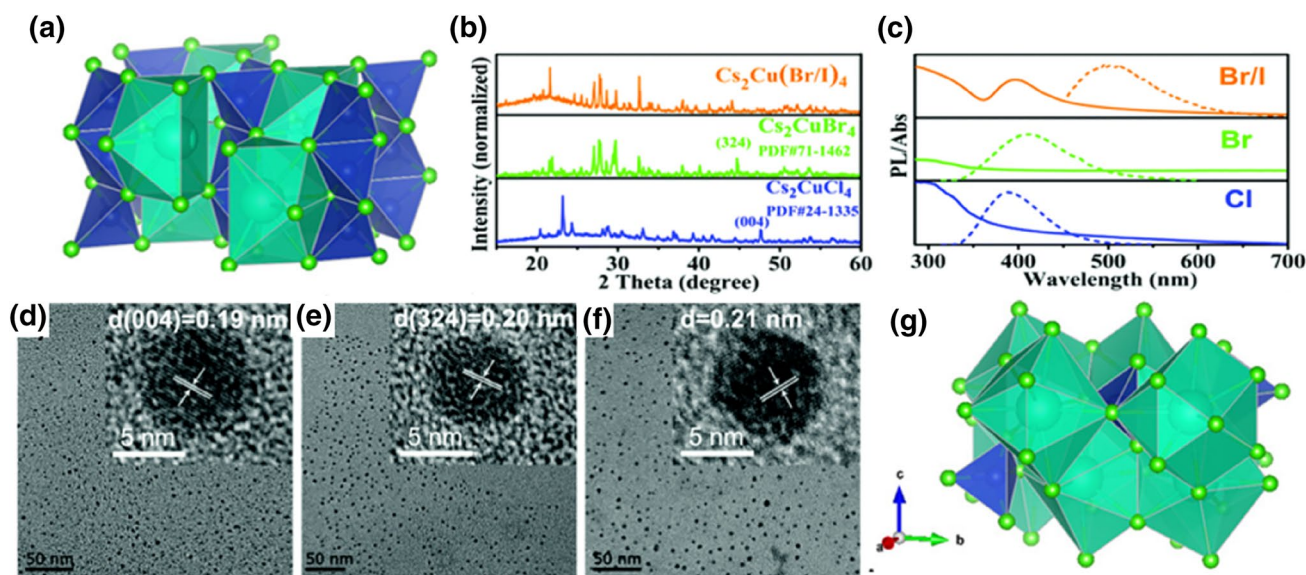


Fig. 8 **a** Structure of Cs_2CuX_4 . Adapted with permission from Ref. [67]. **b** X-ray diffraction patterns of Cs_2CuCl_4 , Cs_2CuBr_4 , and $\text{Cs}_2\text{Cu}(\text{Br/I})_4$ (from bottom to top). Adapted with permission from Ref. [44]. **c** Steady-state absorption and the photoluminescence spectra. Adapted with permission from Ref. [44]. **d–f** Transmission elec-

tron microscopy images of Cs_2CuCl_4 , Cs_2CuBr_4 , and $\text{Cs}_2\text{Cu}(\text{Br/I})_4$; insets: the corresponding high-resolution transmission electron microscopy images. Adapted with permission from Ref. [44]. **g** Illustration of the CmCm crystal structure adopted by the CsCuCl_3 crystals. Adapted with permission from Ref. [67]

during synthesis, to a 1:1 and 1:4 ratio of CsBr and CuBr_2 , respectively. A quasi-spherical shaped QDs with a uniform size of 3.5–3.8 nm in diameter was made by the LARP method at RT (Fig. 8d–f) [44]. The aforementioned findings may be due to the quantum confinement effect considering the size of the QDs based on the precursor ratio [44]. The PLQE of the Cs_2CuCl_4 QDs were as high as 51.8% and the Cs_2CuBr_4 QDs ranged from 32.8 to 37.5%. Both were significantly better values compared with the other LFAIHP QDs. This was due to longer recombination lifetimes suggesting better charge diffusion property than other lead-free perovskite materials [68]. Another important property of Cs_2CuX_4 QDs is their high stability compared with other AIHP QDs including the Pb-based QDs. They retained a PL intensity of 92% after being stored in ambient air for 30 days and 34.2% after illumination under UV light of 5000 m [44]. Improved stability and PLQE are the foundation for practical optoelectronic application.

Booker and his coworkers were able to make CsCuCl_3 QDs by HI method in search for Cs_2CuCl_4 nanocrystals (Fig. 8g) [67]. When the ratio of OA and OLA was 1:4, CsCuCl_3 QDs with average size of 6 nm formed. CsCuCl_3 QDs does not form perovskite structure like CsPbCl_3 but perovskite derived structure with CmCm space group [69]. They had strong PL emission peak at 525 nm equivalent to green luminescence derived from intraband defects, especially Cu(II) defects. The PLQE measured here was too low to be used in practical devices. Since the emission is not derived from intrinsic system such as band to band emission,

it means that the optical properties can be tuned by surface treatment.

3.4 Double perovskite quantum dots

A request for stable LFAIHP lead to an interest in double perovskites which have a formula of $\text{A}_2\text{B}^+\text{B}'^{3+}\text{X}_6$. A site is usually occupied by Cs^+ and unlike other perovskites, the B site is occupied by two types of metals, one monovalent and one trivalent cation, such as Ag^+ , Bi^{3+} , In^{3+} , and Sb^{3+} . Since double perovskites can be easily prepared by replacing two Pb cations with one monovalent and one trivalent metal cation, the perovskite possessed a 3D perovskite structure (Fig. 9a) [70, 71]. The HPs demonstrated improved stability compared with the most widely studied LFAIHP, CsSnX_3 . However, research into the double perovskites is quite novel. Consequently, the optoelectronic properties are not entirely understood and there are virtually no actual devices that have been synthesized with double perovskite quantum dots.

Since the B site is occupied by two types of cations, the production of a pure, single phase double perovskite QDs is quite challenging. Among the various double perovskites, $\text{Cs}_2\text{AgBiX}_6$, and $\text{Cs}_2\text{AgInCl}_6$ are regarded as the most suitable alternative for the Pb-based halide perovskite QDs because of the isoelectronic property of Bi^{3+} and In^{3+} compared with Pb^{2+} . Also, the band gap in the visible area, and the large defect tolerance demonstrates its applicability to photovoltaic devices. As a result, most studies on double perovskites are largely focused on these two materials. These

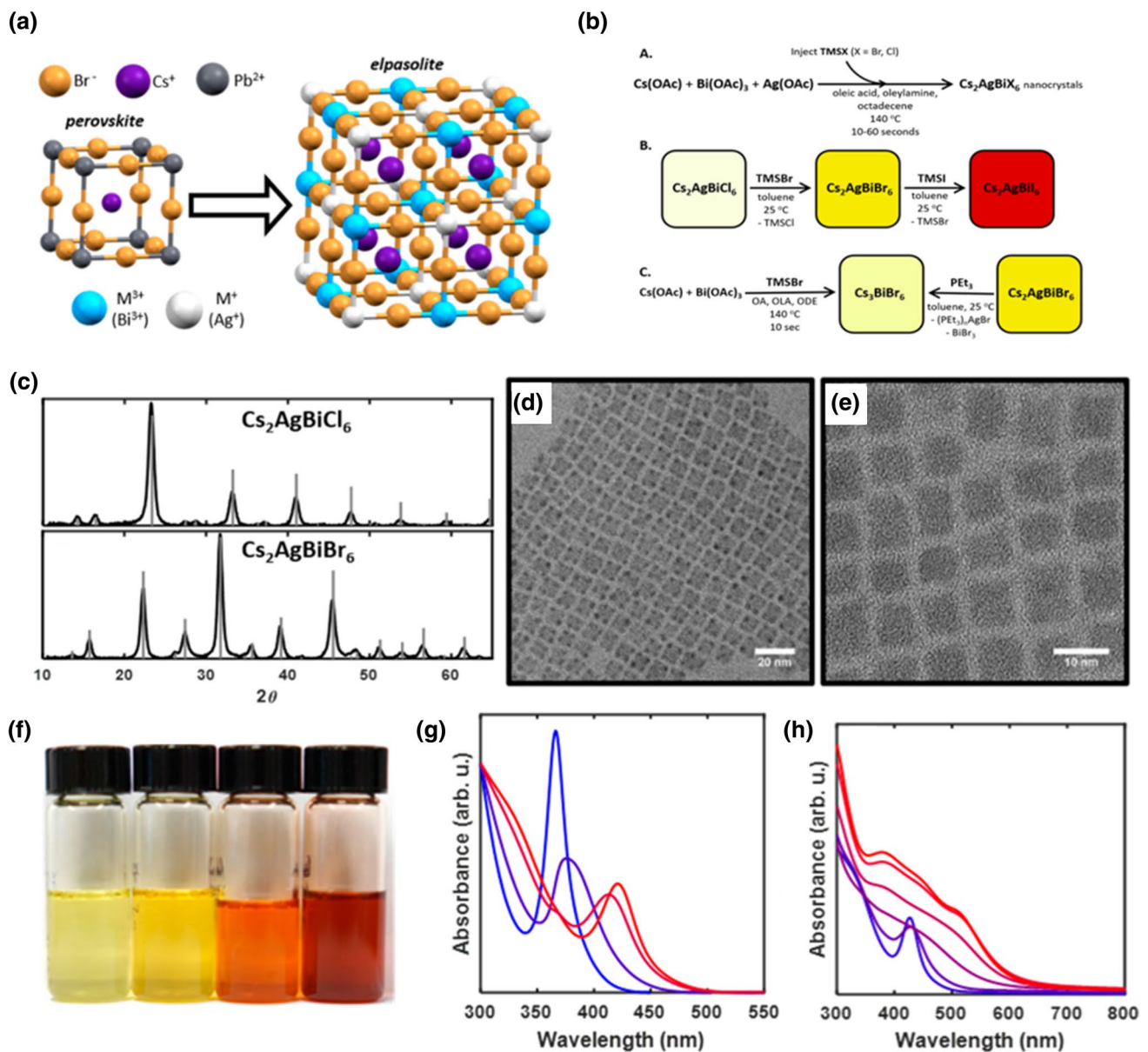


Fig. 9 **a** The elpasolite structure (e.g., $\text{Cs}_2\text{AgBiBr}_6$) can be related to the structure of lead-halide perovskites by the formal doubling of the unit cell dimensions and the replacement of Pb^{2+} with alternating M^+ and M^{3+} cations. **b** Synthesis and reactivity of $\text{Cs}_2\text{AgBiX}_6$ nanocrystals. **d** Transmission electron microscopy characterization of $\text{Cs}_2\text{AgBiCl}_6$. **c** Powder X-ray diffraction patterns (black) for the ~ 13 nm nanocrystals of $\text{Cs}_2\text{AgBiCl}_6$ and $\text{Cs}_2\text{AgBiBr}_6$ compared to the standard diffraction patterns for these materials (gray lines, ICSD Coll. Codes 239,874 and 239,875). **e** Transmission electron

microscopy characterization of $\text{Cs}_2\text{AgBiBr}_6$. **f** Photograph of the dilute toluene solutions of (L–R) $\text{Cs}_2\text{AgBiBr}_6$, $\text{Cs}_2\text{AgBiBr}_{5.2}\text{I}_{0.8}$, $\text{Cs}_2\text{AgBiBr}_{1.6}\text{I}_{4.4}$, and $\text{Cs}_2\text{AgBiI}_6$ nanocrystals. **g** Absorption spectra illustrating the conversion of the $\text{Cs}_2\text{AgBiCl}_6$ nanocrystals to $\text{Cs}_2\text{AgBiBr}_6$ nanocrystals by treatment with increasing amounts of TMSBr (reaction progresses from blue to red). **h** Absorption spectra illustrating the conversion of $\text{Cs}_2\text{AgBiBr}_6$ nanocrystals to $\text{Cs}_2\text{AgBiI}_6$ nanocrystals by treatment with increasing amounts of TMSI (reaction progresses from blue to red). Adapted with permission from Ref. [37]

were the only materials that were able to be successfully made into QDs [21, 22, 37, 72, 73].

Creutz et al. [37] reported the first success in synthesizing $\text{Cs}_2\text{AgBiX}_6$ QDs through the HI method (Fig. 9b, c). The ratio of the precursors, OA/OLA ligand ratio, injection temperature and reaction time were addressed carefully. If one

of these parameters is slightly different from the intended value, then impurities including AgX , CsX , and Cs-Ag-X , appeared. By the post synthetic anion exchange reaction or by changing the precursor material, they could produce the $\text{Cs}_2\text{AgBiX}_6$ QDs with various halide compositions. By tuning the halide composition of these QDs, the emission band

could be tuned from 1.68 to 1.92 eV (Fig. 9g, h). The synthesized $\text{Cs}_2\text{AgBiCl}_6$ and $\text{Cs}_2\text{AgBiBr}_6$ QDs had an average size of 8 nm in edge length with a cubic shape (Fig. 9d, e). Interestingly, while $\text{Cs}_2\text{AgBiI}_6$ was not able to be made in its bulk form due to its low thermodynamic stability, it exhibited a uniform cubic shape in its QD morphology. The reason behind this is not covered in this review and requires further study. Two more successive studies of the $\text{Cs}_2\text{AgBiBr}_6$ QDs were reported by Zhou et al., [21] and Bekenstein et al. [22]. Both groups explored a similar HI method for the synthesis except that they used different materials as precursors. The former group used BiBr_3 , AgNO_3 , and Cs-oleate with OA and OLA as the ligands and HBr as the additive to fully ionize the Ag^+ and suppress the AgBr impurity. In the latter group, the AgBr, BiBr_3 , and Cs-oleate were used as metal precursors. The reaction time was longer for the latter group. A sharp absorption peak around 430 nm was observed in both works. This peak had a large blue shift compared with the bulk $\text{Cs}_2\text{AgBiBr}_6$ [50]. The two groups attributed this phenomenon to different reasons. Whereas Zhou [3] attributed the blue shift to the quantum confinement effect, Bekenstein et al. [22] explained the shift by the localized Bi 6 s-6p transition. As a result, there is a clear indication that more studies are required for a clear understanding of the optical mechanism. The high stability of the double perovskite QDs was confirmed in Zhou's work [21]. Even after washing the $\text{Cs}_2\text{AgBiBr}_6$ QDs in ethanol, which signified decreased amounts of ligands to protect the QDs, the stability was still high, such that no evident decomposition occurred after storing in 55% humidity for 90 days, illuminating by 70 mW cm^{-2} light for 500 h, and heating at 100°C for 30 h. Also, they showed that it is a promising photocatalytic material. This is covered in detail in Sect. 4.4. Further increase in the stability is required for practical use in the device and Bekenstein et al. [22] studied the degradation mechanism of the $\text{Cs}_2\text{AgBiBr}_6$ QDs. In addition to the diffusion and coalescence of Ag, the decomposition into Cs_2BiBr_6 and $\text{Cs}_3\text{Bi}_2\text{Br}_9$ is a main factor for the degradation of the $\text{Cs}_2\text{AgBiBr}_6$ QDs. The degradation could be slowed down by drying. $\text{Cs}_2\text{AgBiBr}_6$ QDs were also able to be synthesized by the LARP method [73]. The $\text{Cs}_2\text{AgBiBr}_6$ QDs synthesized by Yang et al. [73] had an average diameter of 5 nm with a quasi-spherical shape. The $\text{Cs}_2\text{AgBiCl}_6$ QDs showed a PLQE of 6.7% and that increased to 8% by passivating the QDs with an OA ligand. This demonstrated that surface defects had an adverse effect on PL by forming a sub-band trapping site.

Another promising double perovskite material, $\text{Cs}_2\text{AgInCl}_6$ QDs are reported by Locardi et al. [72]. They used the HI method using the metal carboxylate as precursors, and OA and OLA as the ligands. Benzoyl chloride was used as the halide precursor material. The synthesized QDs had a cubic shape and the average edge length was 9.8 nm.

It showed a white emission with a broad spectrum and a PLQE of 1.5%. By doping Mn into the $\text{Cs}_2\text{AgInCl}_6$ QDs, the emission changed to a bright orange emission with a PLQE of 16%.

4 Applications

Owing to the good optoelectronic properties of the LFAIHP QDs, they are expected to be used in a variety of devices such as solar cells, light-emitting diodes (LEDs), photodetectors, photocatalysis and memory devices. Since the emergence of LFAIHP is rather new, more research needs to be conducted to understand the exact optoelectronic properties and to determine the practicality of LFAIHP QDs in real devices. However, we still will cover their potential as alternatives for existing materials and provide examples of their established applications.

4.1 Solar cells

The application in solar cells is one of the most studied area for halide perovskites. A typical structure of solar cells based on halide perovskite quantum dots is shown in Fig. 10. Unfortunately, there are no studies thus far that report a solar cell that is fabricated with LFAIHP QDs. However, there are reports of solar cells based on the Pb-based AIHP QDs, achieving a solar cell efficiency of 13.43% [74, 75]. The solar cell fabricated with CsPbI_2 quantum dots and CsPbBrI_3 layer showed the best performance among lead-based halide perovskite quantum dot solar cells. It showed open circuit voltage (V_{oc}) of 1.204 V, short circuit current (J_{sc}) of 15.25 mA cm^{-2} , 78.7% fill factor (FF), and 14.45% power conversion efficiency (PCE) [124]. In search of other materials, Shen et al. [76] reported Pb-substituted $\text{CsSn}_{1-x}\text{Pb}_x\text{I}_3$ QDs by alloying CsPbI_3 and CsSnI_3 and demonstrated its potential to be used in solar cells. It showed a better phase stability than both the CsPbI_3 and CsSnI_3 QDs which mainly restricts the inorganic HP QDs from solar cell applications. Ultrafast transient absorption spectroscopy revealed that

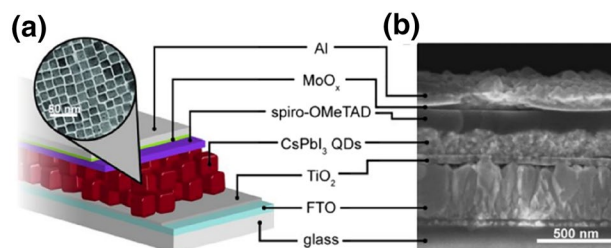


Fig. 10 **a** Schematic (with transmission electron microscopy image of QDs) and **b** Scanning electron microscopy image of cross-section of the CsPbI_3 -based solar cell. Adapted with permission from Ref. [75]

electrons formed by photoexcitation in the alloyed QDs can be injected into the charge collection layer at a rate of $1.12 \times 10^{11} \text{ s}^{-1}$, thus leading to the high photocurrent generation in solar cells.

Some lead-free materials are arising as alternatives to be used in solar cells because of the toxicity and carcinogenicity of lead. CsSnI_3 is considered to be a promising material due to the small band gap of 1.3 eV which is an ideal value for single-junction solar cells [77]. It was found that the open circuit voltage (V_{oc}) of the CsSnI_3 based solar cell is limited by the Shockley–Read–Hall recombination in the absorber layer itself [115]. Hatton et al. [77] showed that the main determinant of V_{oc} is the energetics at the interface between CsSnI_3 and ETL. As mentioned in Sect. 2, CsSnI_3 has a low stability, which did not allow the CsSnI_3 -based solar cell to be of practical use. Recently, Padutre et al. [78] made an advance in the fabrication of efficient and stable lead-free inorganic perovskite solar cells. They used $\text{CsSn}_{0.5}\text{Ge}_{0.5}\text{I}_3$ as a light-absorber with a 5 nm thick native-oxide Ge(IV) layer on top. By forming a thin protective layer above the absorber layer, the full encapsulation and passivation of the perovskite surface was possible, thereby resulting in a decrease in the electron and hole trap densities in the halide perovskite to as low as 10^{16} cm^{-3} . High stability, with less than 10% decrease in efficiency, occurred after a 500 h operation and a high efficiency of 7.11% was achieved in this solar cell.

Double perovskites are another promising material to be applied in solar cell because of their superior phase stability, small charge carrier mass, and low exciton binding energy. Among 350 different double perovskites, Cs_2SnI_6 [79], Cs_2TiBr_6 [80], and $\text{Cs}_2\text{AgBiBr}_6$ [22] are regarded as the most suitable, based on the band gap. Cs_2SnI_6 has a band gap of 1.48 eV and high absorption coefficient of 10^5 cm^{-1} . The first solar cell using Cs_2SnI_6 as the absorber layer, and a ZnO nanorod as the electron transport layer was reported by Cao et al. [81] By adjusting the thickness of Cs_2SnI_6 , Kanatzidis et al. [82] was able to synthesize a solar cell with a V_{oc} of 0.51 V, a power conversion efficiency (PCE) of 1%, and a J_{sc} of 5.41 mA cm^{-2} . A Cs_2TiBr_6 thin film based solar cell was fabricated by Chen et al. [83] that exhibited an appropriate band gap of 1.8 eV, long carrier diffusion length greater than 100 nm, and an outstanding stability with regard to moisture, heat and light. In addition, this solar cell achieved up to 3.3% stable efficiency. The $\text{Cs}_2\text{AgBiBr}_6$ exhibited an indirect band gap of 1.95 eV in the visible range is the most studied double perovskite and demonstrates the potential to be used as a tandem solar cell [50, 84]. Due to isoelectronic nature of Bi^{3+} and Pb^{2+} resulting in a high defect-tolerance [70, 85] and high carrier density of $2.2 \times 10^{16} \text{ cm}^{-3}$, an efficient charge formation and transport are expected for the $\text{Cs}_2\text{AgBiBr}_6$ -based solar cells [86]. The first $\text{Cs}_2\text{AgBiBr}_6$ based solar cell was fabricated by Xiao et al. [87], and the device showed a PCE of up to 1.44%. Further increase in

the PCE up to 2.5% with a V_{oc} more than 1 V was achieved in the work of Bein et al. [84], even without encapsulation.

QDs usually have symmetric crystal structures contributing to the low surface energy. Considering the large surface to volume ratio, when the previously mentioned materials with the QD shape can stably form the absorber layer, higher PCE and V_{oc} with superior stability is expected. In particular, ligands should be addressed carefully although ligands are advantageous for stability, they have disadvantageous effects on the fill factor (FF) and other photovoltaic values by hindering charge transport and decreasing the coupling between QDs [14]. Therefore, studies on the manufacture of QDs without ligands while maintaining the QD distribution, should be conducted to fabricate practical LFAIHP QD-based solar cells.

4.2 Light emitting diodes (LEDs)

LEDs are another commonly studied area for the application of AIHP QDs. In LEDs, the material needs to display the emission peak in the range of visible light. Also, high photoluminescence (PL) intensity and small FWHM are required for high brightness and high color purity. Also, since LEDs are used physically close to humans, the non-toxicity of LEDs is necessary. Studies based on the Pb-based perovskite quantum dots have been conducted [2, 21, 88]. They showed promising values and demonstrated that AIHP QDs have a high potential to replace existing semiconductor materials. An LED device fabricated with $\text{CsPbBr}_{0.6}\text{I}_{2.4}$ showed best external quantum efficiency (EQE) of 21.3% which was the best among lead-based halide perovskite quantum dot LEDs [125]. It showed current efficiency (CE) of 66.7 cd A^{-1} and max luminance of $76,940 \text{ cd m}^{-2}$ [126]. However, in terms of the toxicity, the Pb-based material is not suitable. Several materials show potential to replace the Pb-based QDs.

In 2018, Leng et al. [41] manufactured the $\text{Cs}_3\text{Bi}_2\text{X}_9$ perovskite QDs and fabricated a white light-emitting diode (W-LED). The $\text{Cs}_3\text{Bi}_2\text{X}_9$ colloidal QDs with a diameter of 3.88 nm were synthesized by LARP, using ethanol as the main solvent. It was verified that by changing the halide composition of the perovskite by using different precursors during synthesis, the photoluminescence peak can be tuned from 393 to 545 nm. A blue emission peak at 410 nm with a PLQE of 19.4%, FWHM of 48 nm, and a small stokes shift of 15 nm was observed in the as-synthesized colloidal $\text{Cs}_3\text{Bi}_2\text{X}_9$ QDs (Fig. 11a). The observed optical properties showed that the $\text{Cs}_3\text{Bi}_2\text{X}_9$ perovskite QDs are promising materials for actual LEDs. Compared to the existing Pb-based perovskite QDs with similar emission wavelengths, the observed PLQE of $\text{Cs}_3\text{Bi}_2\text{Br}_9$ was higher, or at least comparable. Specifically, the all-inorganic Pb-based CsPbCl_3 QDs with an emission wavelength of 405 nm showed a 10% PLQE, [21] and organic–inorganic hybrid $\text{PEA}_2\text{PbBr}_4$

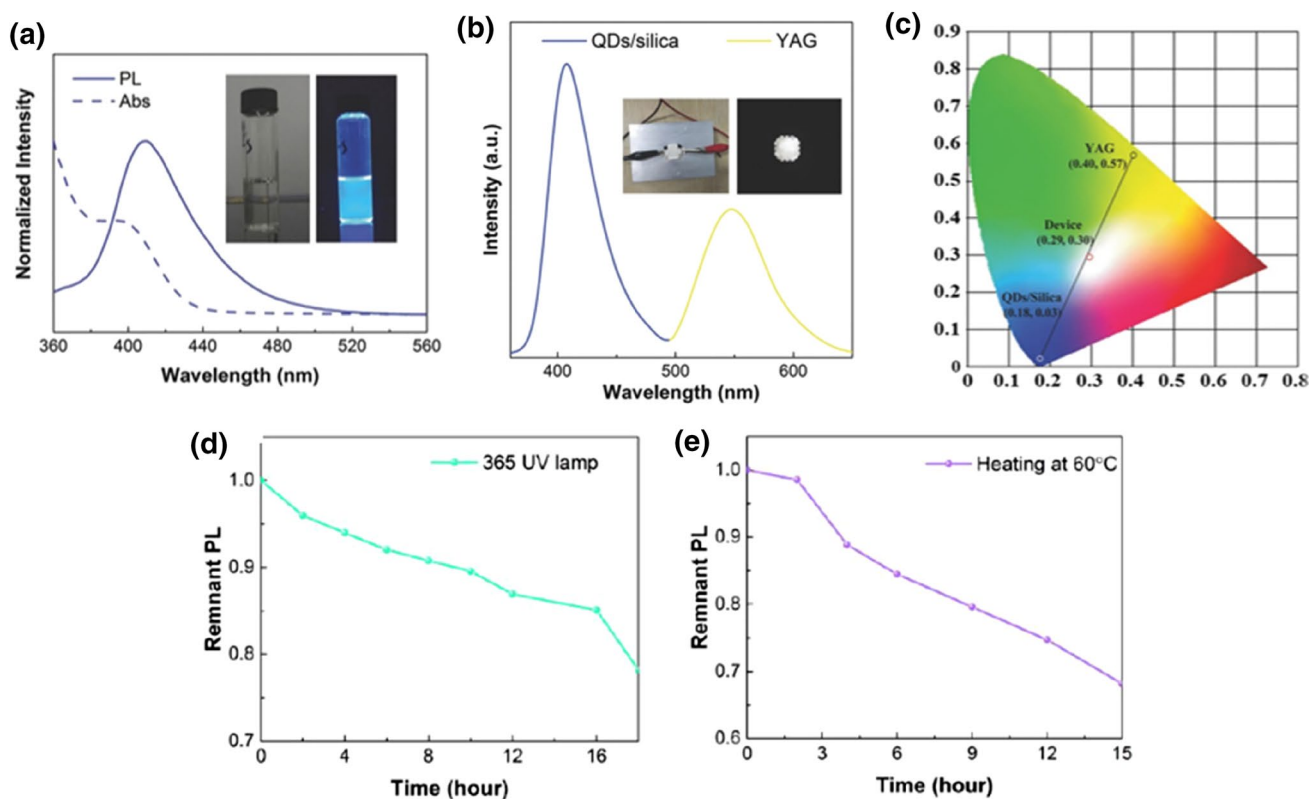


Fig. 11 **a** Absorption and PL Spectra of $\text{Cs}_3\text{Bi}_2\text{Br}_9$ QDs. Insets: Typical optical images of the QD solution in ambient air under a 325 nm UV lamp illumination. **b** EL spectrum of the W-LED by combing blue-emissive $\text{Cs}_3\text{Bi}_2\text{Br}_9$ QDs and yellow-emissive rare-earth phosphor YAG. Inset: Device images of the QD/silica composites com-

pared with YAG (off and on). **c** CIE color coordinates corresponding to the $\text{Cs}_3\text{Bi}_2\text{Br}_9$ QDs, YAG, and W-LED (**d**), **e** Photostability (under 365 nm UV lamp) and thermal stability (under heating at 60 °C) of W-LED device. Adapted with permission from Ref. [41]

perovskite QDs (PEA: $\text{C}_6\text{H}_5\text{CH}_2\text{CH}_2\text{NH}_3$) with an emission peak of 410 nm showed a 26% PLQE [118]. The stability issue, which is the main problem hindering LFAIHP QDs from practical applications also took a step forward by BiOBr passivation. The passivated $\text{Cs}_3\text{Bi}_2\text{Br}_9$ perovskite QDs only showed a 20% reduction in PL intensity under the illumination of 78 h, and a 10% reduction after 8 h storage in DI water [41]. Based on these excellent properties, they fabricated W-LED using blue-emissive $\text{Cs}_3\text{Bi}_2\text{Br}_9$ QDs and yellow-emissive $\text{Y}_3\text{Al}_5\text{O}_{12}$ (YAG) (Fig. 11b). The $\text{Cs}_3\text{Bi}_2\text{Br}_9$ QDs/silica composite powder and YAG phosphor powder were mixed with a mass ratio of 10:1 followed by a simple painting process of powder on a GaN chip. The as-fabricated W-LED had Commission International de L'Eclairage (CIE) color coordinates of (0.29, 0.30) which suggests white light (Fig. 11c). It also had satisfactory stability and the device showed 78% of the initial PL after illumination of 16 h and 68% of the initial PL after heating at 60 °C for 15 h (Fig. 11d, e).

CsSnX_3 , $\text{Cs}_3\text{Bi}_2\text{X}_9$, or Cs_2CuX_4 has a potential to be used as LEDs. In the work of Jellicoe et al.,²³⁾ the emission peak of CsSnX_3 could be tuned from 470 to 930 nm by changing

the halide type which means that it can cover red to blue LEDs. Yang et al. [43] successfully synthesized $\text{Cs}_3\text{Bi}_2\text{X}_9$ QDs and showed that by changing the halide composition, $\text{Cs}_3\text{Bi}_2\text{X}_9$ can cover from 400 to 560 nm [43]. In a more recent study, Cs_2CuX_4 was also able to change its emission peak from 385 to 504 nm by changing the halide composition [44]. However, a major challenge arises during the manipulation of the wavelength of luminescence. When two types of halide ions are mixed to generate a luminescence of in-between wavelength, the halide exchange occurs constantly, thereby resulting in an unstable emission peak and fast degradation.

There is no doubt that QD is a more appropriate morphology than the bulk for fabricating efficient LEDs. Due to the high overlap of electron–hole wavefunctions, and the decreased number of the unfilled trap states of QDs compared with the polycrystalline film, the QDs show enhanced photoluminescence (PL) and electroluminescence (EL) efficiencies under low excitation density or applied bias [89, 90]. In addition, the small size of QDs can trigger an exciton confinement and the increase exciton binding energy, thus leading to more radiative exciton recombination and a

decline in the non-radiative free carrier recombination [46, 91, 92]. In addition, the small size contributes to less sub-band defect states when the surface of the QDs is well passivated [93, 94]. From studies on CsPbX₃ QD-based LEDs, we can find a way to achieve a highly efficient and stable LED with the LFAIHP QDs. QD film control or control on separate QDs would passivate the surface and impact the efficiency and stability of the LED [95]. Encapsulating the QDs with the polymer matrix [96], changing conventional OA, OLA ligands with stronger binding [97] or larger steric hindrance ligands [98] or overcoating QDs [99] might enable the fabrication of the practical LFAIHP QD-based LED.

4.3 Photodetectors

There are some factors to be considered for a photodetector to show good device performance, such as the generation and separation of the photocarrier, collection and transportation of the charge carrier, and resistance and capacitance of the system [100]. The generation and separation of photocarrier is mainly determined by the structure of the device. Specifically, while the conventional photovoltaic detectors have built-in electric fields that lead to enhanced generation and separation of photocarriers, the metal–semiconductor–metal (MSM) structure, that is usually adopted for photodetectors fabricated with inorganic halide perovskites as the absorber does not show a built-in electric field. Since the material has negligible influence when compared with the structure of the device, the generation and separation of the photocarriers are not the focus of this review [101]. Control over the charge carrier is strongly dependent on the grain size of the perovskite absorber layer [100, 101]. In a photodetector, the photogenerated carriers are trapped by the defects formed by the interfacial areas between the grains, thus signifying a slow photoresponse time. Therefore, the improvement of the photoresponse time and the photoresponsivity is expected when the perovskite absorber layer is formed by particles of smaller size like QDs, due to the decreased grain boundaries, which indicate a low defect state density, longer lifetime of photocarriers, and a small recombination rate. Manufacturing the perovskite absorber layer with QDs influences not only the transportation of carriers but also the collection of carriers. The collection process is largely influenced by the electrode distance and the semiconductor contact. Since QDs can form monolayer film, controlling the thickness of the absorber layer is easier than controlling the bulk material. In addition, the wide variety of methods for surface treatment demonstrate multiple ways to control the behavior between the semiconductor/metal interface.

However, reports of photodetector with the all-inorganic halide perovskite are scarce. There is only one photodetector that has been fabricated with CsPbX₃ QDs as the absorber layer, reported by Lu et al. [7]. The

fabricated photodetector had a very short photoresponse time of 0.48/1.03 ms, which corresponded to the rise/fall response time. A high responsivity of 54 mA W⁻¹ was also observed. The LFAIHP materials with high potential applicability to photodetectors are Cs₂SnI₆ [32], Cs₂AgBiBr₆ [102, 103], and Cs₃Sb₂X₉ [46]. In the work of Ghosh et al. [32], photo-switching behavior was observed for various Cs₂SnI₆ nanostructures such as nanosheets, nanocubes, and nanorods (Fig. 12a). The Cs₂SnI₆ in a nanorod demonstrated the maximum on/off ratio of 475 which was a superior value compared to that of the nanosheets and nanocubes, which were 20 and 14.5, respectively, at a 5 V bias (Fig. 12b). Furthermore, the response in a nanorod system was found to be superior compared with nanosheet or nanocube systems due to the fast carrier migration arising from the 1D morphology. It took under 2 s to achieve the maximum photocurrent value in the nanorod system, whereas up to 20 s were required for the nanosheet and nanocube systems; this implies that a 0D morphology, consequently QDs, are more suitable for photodetectors. The Cs₂AgBiBr₆ thin film-based photodetectors were fabricated by Lei et al., [102] and Wu et al. [103]. In the work of Lei et al. [102], MSM structure photodetector using Au as a metal electrode was fabricated. The photoresponsivity was maximized at 510 nm with a value of 7.01 A/W. Other parameters such as the on/off current ratio, detectivity, and external quantum efficiency (EQE) were also measured at 2.16×10^4 and 5.66×10^{11} Jones. An extremely short response time was observed at 50 Hz, which was 5.77/5.97 ms for the rise/fall time. However, a better rise/fall time of 956/995 μs was observed at 500 Hz [102]. Another Cs₂AgBiBr₆ thin film-based photodetectors were made by Wu et al., which can be self-powered [103]. The device structure was ITO/SnO₂/Cs₂AgBiBr₆/Au with the absence of a hole-transport layer. The responsivity peak was observed at two points, first at 350 and then at 435 nm. The superior values compared with other oxide heterojunction-based photodetectors for ultraviolet light were observed. The response time was less than 3 ms and the responsivity was as high as 0.11 A/W at the 350 nm peak. It was attributed to the efficient transportation of the charge carrier at the interface between SnO₂ and Cs₂AgBiBr₆ in addition to the high integrity of the perovskite thin film. Also, Cs₂AgBiBr₆ possesses a good stability with regard to moisture and illumination, which is confirmed by researches in Sect. 3.4. Considering all these properties, the fabricated photodetector indicates the promising qualification of the Cs₂AgBiBr₆-based photodetector. The Cs₃Sb₂X₉ nanowire-based photodetector was made by Pradhan et al. [46]. The length of the colloiddally synthesized Cs₃Sb₂X₉ nanowires was able to be tuned by changing the precursor and ligand ratios. The fabricated photodetector from the Cs₃Sb₂X₉ nanowires had an

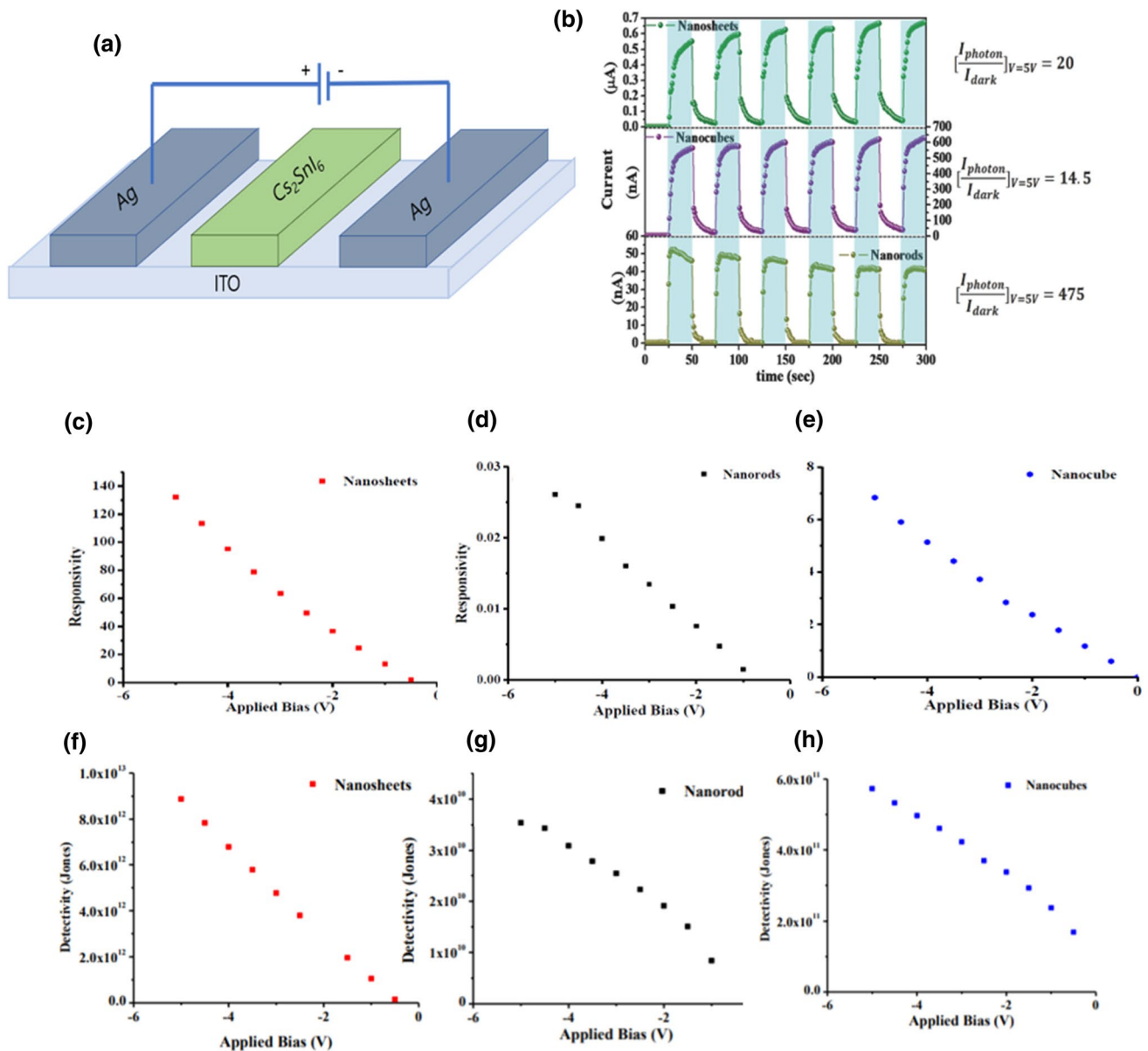


Fig. 12 **a** Schematic diagram of the photoresponse device. **b** Photoswitching behavior of different nanostructures at a bias voltage of 5 V. Combined plot of the responsivity (**c–e**) and detectivity (**f–h**) of

nanosheets, nanorods and nanocubes at a variable bias. Adapted with permission from Ref. [32]

MSM structure using Au as the metal electrode and the distance between metals was 100 nm. At a 0.9 V bias, the rise and fall time was 0.13 and 0.23 s, respectively. It showed almost no decay in photocurrent while maintaining a high photosensitivity, even after repetitive switching cycles, thus indicating the good photostability of the material. Additional research is required for the manufacture of practical LFAIHP QDs-based photodetectors since even the material in the QD morphology itself is not fully understood. However, it seems clear that LFAIHP QDs would be a novel material for photodetectors in the future.

4.4 Photocatalysis

Mostly, the application in photovoltaics is a major concern for AIHP QDs and the photochemical conversion device application is a less studied area because of the insufficient stability to moisture or polar solvents [104]. For that reason, the application in photocatalysis is a relatively less mentioned area compared to the earlier mentioned LEDs, solar cell, and photodetector. However, it is undoubtedly an interesting topic because of the outstanding photophysical properties, including long charge diffusion lengths, high charge

carrier mobility, high absorption coefficient, tunable band gap and broad absorption spectrum [95]. The photocatalytic application of AHP QDs were first suggested by Kuang et al. [104] in 2017. They discovered that the CsPbBr₃ QDs can trigger photocatalytic CO₂ reduction at a rate of 23.7 μmol/g h with a high selectivity of 99.3% by constantly generating and injecting electrons into the CO₂. The rate of electron consumption was further increased by the manufacturing of the CsPbBr₃ QDs/graphene oxide composite because of the enhanced electron extraction and transport [104].

The photocatalytic application was extended to LFAHP QDs. In the work of Zhou et al. [21], the Cs₂AgBiBr₆ double perovskite QDs showed CO₂ catalytic reaction with better stability compared with previously reported CsPbBr₃ QDs-based photocatalytic devices, no evident material decomposition after storing in 55% relative humidity for 90 days, able to sustain 100 °C for 300 h, and no phase transition under constant 150 W LED illumination of 500 h. The electron consumption rate was 105 μmol/g (6 h) and the selectivity was 100%, since there was no H₂ evolution unlike in the case of CsPbBr₃. Although the electron consumption rate is poor compared with the rate achieved for other reported semiconductor photocatalysts, the environmentally friendly characteristic and improved stability lay the foundation for the LFAHP QDs in photocatalytic application (Fig. 13).

Despite the successful demonstration of LFAHP QDs in photocatalysis, it still requires further improvement to be able to be applied in practical devices [95]. First, the low stability in polar solvents must be solved. The previously mentioned photocatalytic phenomenon was possible only in ethyl acetate and the stability in water or alcohol is not confirmed, since there are no reports that suggest that LFAHP QDs can be dispersed in water. This causes additional complications that, when photocatalytic reaction occurs in nonpolar solvents containing carbon, CO or CH₄ can be generated from the solvent rather than the intended reaction. These unwanted reactions can limit the productivity. Second, the recombination of photogenerated charge carriers is so high that it cannot use charge carriers effectively, thus leading to poor efficiency. Investigations into the more wide-band gap materials or the manufacture of the core-shell nanostructure might be the solution to these problems by charge separation and improved stability [95].

4.5 Electronic devices

The need for new memory devices that can store increasing amounts of information lead researchers to discover new materials other than the conventional semiconductors, or metal oxides. Halide perovskites have some interesting properties that make them suitable to be used in memory devices, such as fast ion migration, superior control over the majority carrier and flexibility [105–107]. The

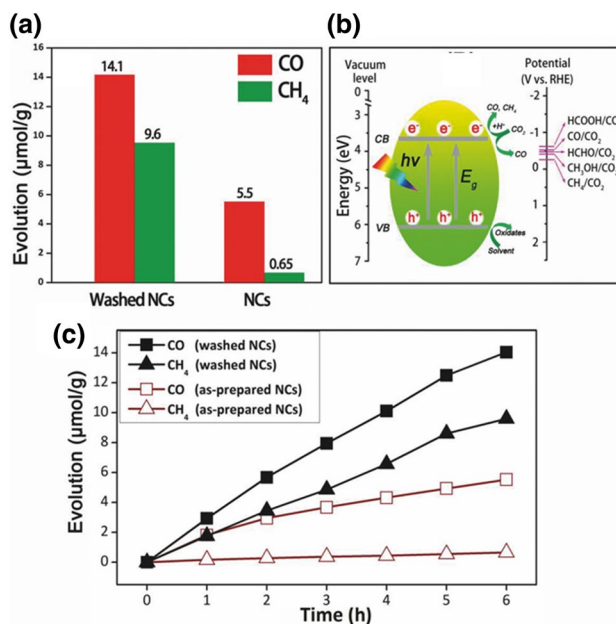


Fig. 13 **a** Comparison of the photocatalytic CO₂ reduction performance of the as-prepared Cs₂AgBiBr₆ NCs and the washed NCs. **b** Schematic diagram of the photoreduction of CO₂ on the surface of Cs₂AgBiBr₆ NCs. **c** Time course of CO and CH₄ evolutions for the as-prepared and washed Cs₂AgBiBr₆ NCs. Adapted with permission from Ref. [21]

demand for a smaller size, together with non-toxicity make LFAHP promising for this application. Currently, reports on the use all-inorganic halide perovskite is limited, particularly with Pb-free materials. Wang et al. [34] synthesized Cs₂SnI₆ nanobelts by the HI method and employed it to make a field effect transistor (FET). Since the material is colloidal synthesized, the nanobelt film was easily formed by spin coating the solution (Fig. 14). The fabricated FET demonstrated excellent performance, showing p-type conduction with a high hole mobility of more than 20 cm²/Vs, a hole concentration of 9.1 × 10¹⁸ cm⁻³, and a high on/off ratio of more than 10⁴. The measured hole mobility was higher than that recently reported for the FET based on PbSe, ZnTe, or CdSe/ZnS nanocrystals. In addition, it was comparable to the optimum value of organic FETs. The fact that these properties were not negatively impacted, even after two weeks of exposure to ambient air, demonstrates the stability of Cs₂SnI₆ nanocrystals in an actual device. In 2018, the first resistive switching memory based on Pb-based all-inorganic halide perovskite QDs (CsPbBr₃ QDs) was fabricated [9]. Compared to the device based on bulk CsPbBr₃, the device based on CsPbBr₃ QDs showed 100 times the endurance, 1000 times the on/off ratio, and consumed 100 times less power. These reports support the possible use of LFAHP QDs as materials for future memory devices.

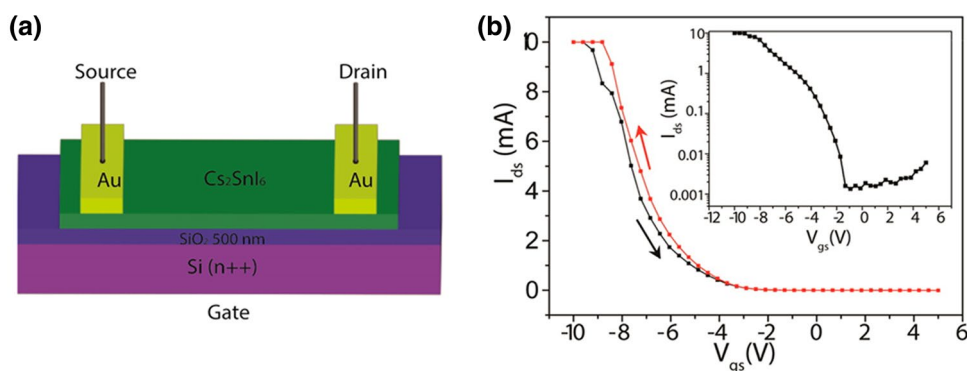


Fig. 14 **a** Schematic illustration of the field effect transistor device configuration using Cs_2SnI_6 nanobelts as the channel materials measured under ambient conditions. **b** Linear plot of the $I-V$ characteristics at a drain- source voltage ($V_{ds}=10$ mV). The black and red

lines are positive scan and negative scans, respectively. The inset at **b** gives the $I_{ds}-V_{gs}$ curve on the natural logarithmic scale. Copyright Adapted with permission from Ref. [34]

5 Outlook

5.1 Engineering composition of perovskites

The two main challenges that limit the practical application of LFAIHP QDs are its low quantum yield (QY) and stability compared with Pb-based AIHP or traditional metal chalcogenide QDs. LFAIHPs have a poor power conversion efficiency (PCE) due to their short carrier diffusion length and low carrier mobility. The fact that most LFAIHPs have indirect band gaps, rather than direct band gaps, indicates that LFAIHPs do not readily demonstrate good device performance. While the efficient absorption of light and radiative emission occurs mainly through the photons with a high absorption coefficient and fast carrier-charge recombination, which result in a high PLQE in the direct band gap system, there is a significant interaction between the phonons-photons which negatively influences the photophysical process [8].

One of the promising ways to overcome this problem is by partially substituting the B-site metal cation with another metal cation by doping or alloying. The material that originally has an indirect band gap could be converted to one with a direct band gap by this method [108, 109]. Yang et al. [109] was able to synthesize the first LFAIHP QD with a direct band gap by alloying Bi and In in the LARP process (Fig. 15a). The band gap of the $\text{Cs}_2\text{AgIn}_x\text{Bi}_{1-x}\text{Cl}_6$ QDs was tuned by the x value (Fig. 15b, d–f). The x value was determined by controlling the ratio of BiCl_3 and InCl_3 in the precursor solution. When x reached 0.75, the band gap changed from indirect to direct. The $\text{Cs}_2\text{AgIn}_{0.75}\text{Bi}_{0.25}\text{Cl}_6$ with a direct band gap showed greatly enhanced optical properties compared with the $\text{Cs}_2\text{AgBiCl}_6$ double perovskite with an indirect band gap. Specifically, the $\text{Cs}_2\text{AgIn}_{0.75}\text{Bi}_{0.25}\text{Cl}_6$ demonstrated thrice the absorption, decreased trap states by sub-bands, and a photoluminescence quantum efficiency

(PLQE) of 36.6%, the last of which was a five-fold increase (Fig. 15c) [109]. As previously mentioned, these properties were attributed to the disappearance of the phonon participation, which is observable in the indirect band gap, thus, leading to strong photon radiative emission which also meant that the trap state transition is negligible. In particular, the increased PLQE was comparable with that of the Pb-based AIHP QDs, thus confirming great potential use of LFAIHP QDs in optoelectronic devices.

Mn^{2+} doping is a well-known method for controlling the electrical properties of semiconducting nanocrystals. Locardi et al. [72], applied this method to $\text{Cs}_2\text{AgInCl}_6$ QDs. Before doping, $\text{Cs}_2\text{AgInCl}_6$ QDs displayed white photoluminescence with a broad spectrum and a QY of $\sim 1.6 \pm 1\%$. When the doping level increased to 1.5%, the emission changed to orange, centered at 620 nm with a PLQE of $16 \pm 4\%$. The orange emission was attributed to the defect state caused by Mn^{2+} impurities. The energy absorbed at the band edge of $\text{Cs}_2\text{AgInCl}_6$ was transferred to the Mn^{2+} impurities and then reemission from this state created the orange emission. An interesting phenomenon observed was that doping was not possible above 1.5%.

5.2 Surface engineering

One factor that hinders the high PLQE and stability of QDs is surface defects. Sub-bands occur mainly from surface defects [105] in QDs and are not an intrinsic property of the material. Sub-bands contribute to the nonradiative recombination of excitons and trap sites of carriers [110]. The degradation of QDs, and the instability of QDs and turning into bulk also arises from defects at the surface. As such, engineering the surface of the QDs is important, where the surface to volume ratio is large, especially for high stability. There are many methods of surface treatment, such as controlling ligands, encapsulation, and making a core-shell

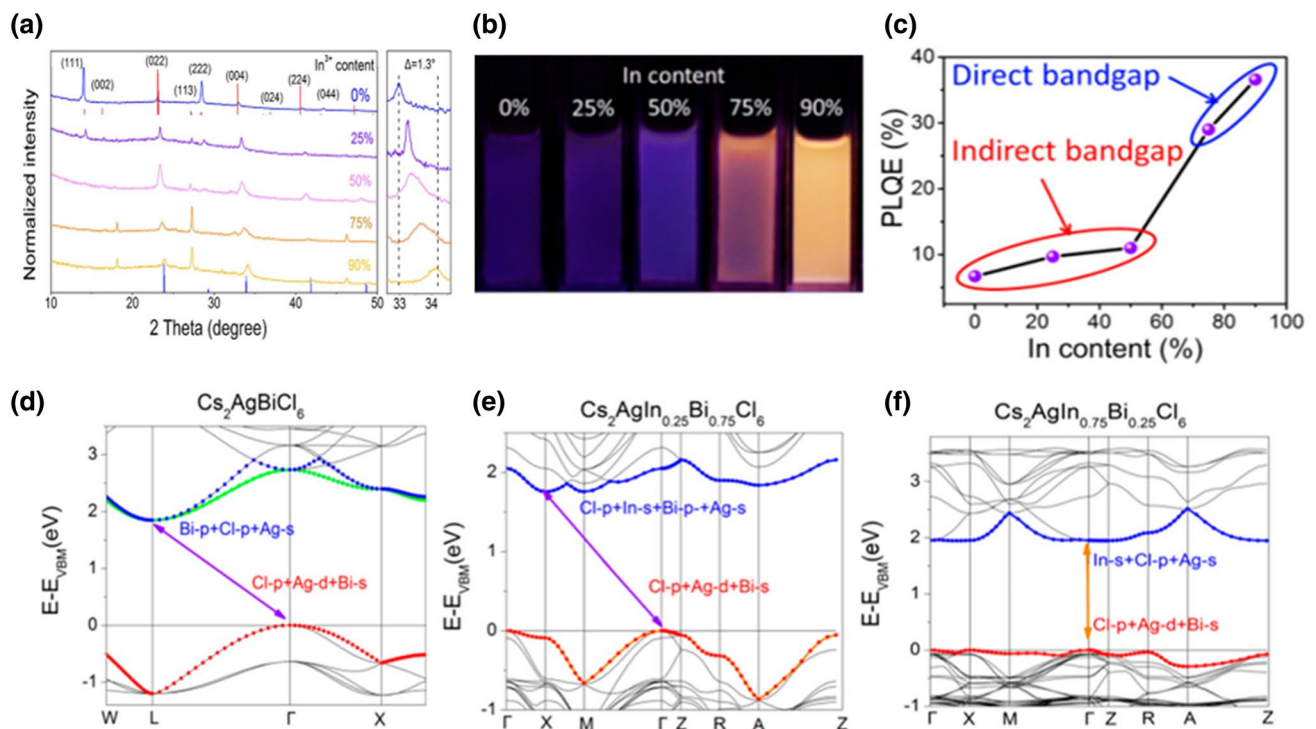


Fig. 15 **a** XRD patterns of $\text{Cs}_2\text{AgIn}_x\text{Bi}_{1-x}\text{Cl}_6$ ($x=0, 0.25, 0.5, 0.75$, and 0.9) NCs (left) and magnified images of XRD patterns (right). Red bar and blue bar represent the XRD patterns of $\text{Cs}_2\text{AgBiCl}_6$ and $\text{Cs}_2\text{AgInCl}_6$ by theoretical calculations, respectively. **b** PL image

of $\text{Cs}_2\text{AgIn}_x\text{Bi}_{1-x}\text{Cl}_6$ under UV light of 365 nm. **c** PLQE value of $\text{Cs}_2\text{AgIn}_x\text{Bi}_{1-x}\text{Cl}_6$ ($x=0, 0.25, 0.5, 0.75$, and 0.9) NCs capped with 8% OA. **d–f** Band structure of $\text{Cs}_2\text{AgIn}_x\text{Bi}_{1-x}\text{Cl}_6$ ($x=0$ (**d**), 0.25 (**e**), and 0.75 (**f**)). Adapted with permission from Ref. [109]

structure. A ligand is a material that is attached to the surface of QDs, passivating the defects and protecting the QDs from the external environment. Moreover, ligands assist the QDs to form well-dispersed layer. Hence, selecting the appropriate ligands is important to facilitate the creation of stable and high QY QDs. The encapsulation of QDs is another promising method to improve stability [19]. Encapsulation protects the QDs from detrimental environmental effects and agglomeration leading to bulk system; therefore, it would be advantageous in LEDs or for fabricating thin films [111]. There are various techniques for encapsulation, including the sol–gel method, usage of a template, physical methods, and microencapsulation [18, 20]. Forming a core–shell structure is another effective way to modify properties of QDs. The latter is the most well-established method and has been extensively used for LEDs with chalcogenide QDs. In this structure, core refers to the QDs for intended use and the shell completely surrounds the core. As a result, the interaction between nanoparticles leading to aggregation is effectively prevented as in the case of encapsulation. Furthermore, the shell reduces the surface defects which form trap states so that non-radiative PL emission is effectively reduced, giving rise to high PLQE. Various types of shells have been adopted with perovskites, especially for MAPbI_3 . According to the material used for the shell, it is classified as

oxide-, semiconductor- (typically using perovskite with different compositions), polymer-, and multilayer shell [112]. These methods have not yet been adapted to LFAIHP QDs. However, there are reports on CsPbBr_3 , suggesting the possibility of using these methods to be used in LFAIHP QDs. Although there are various techniques, we will focus on that of controlling ligands. Although certain techniques, such as core–shell structure can improve the stability of QDs and might be helpful for LED devices, it negatively impacts on devices which require good carrier mobility like solar cell or memory device.

Ligands act to stabilize the surface of QDs and reduce surface defects by combining with dangling bonds [2]. So, making QDs with appropriate ligand is an important step for the practical use. The impact of the ligand is confirmed in $\text{Cs}_3\text{Bi}_2\text{X}_9$ QDs [43]. The PLQE of $\text{Cs}_3\text{Bi}_2\text{Br}_9$ QDs without the ligands was 0.2% which could be improved to 4.5% by adding OA. The stability was also greatly improved by OA. Further, by addition of extra ligands such as OLA [64] or octylammonium [41] along with OA, PLQE of $\text{Cs}_3\text{Bi}_2\text{Br}_9$ QDs further increased up to more than 20%. Ligands can be divided into two types based on how the ligands adsorb to the surface of the QDs [113]; this property is determined by the anchor group involved. One type uses alkyl phosphine (P), alkyl phosphine oxide (RPO), or alkyl amines (R3PO)

which have a lone pair of electrons as the anchor group of ligands; they are weakly bound and are termed *L*-type. The other group, *X*-type, uses covalent bonding to adsorb onto the surface of QD; this results in a strong bond. Typical *X*-type anchor groups are carboxylic acids ($-\text{COOH}$), thiols ($-\text{SH}$), and phosphonic acid ($-\text{PO}_3\text{H}_2$). For the colloidal synthesis of IHP QDs, the purification before the fabrication of the device is essential. During the process, *L*-type ligands are easily detached from the QDs. Hence, the *X*-type ligands are more appropriate for strong attachment. While the weak attachment to the surface occurs in *L*-type ligands, protection from the external environment, such as moisture is much more efficient than *X*-type because they possess carbon chains in three directions. This means that the *X*-type ligand is useful for reducing surface defects, improving stability and QY and the *L*-type is effective for improving stability in the environment. The importance of choosing an appropriate ligand is well documented in CsPbBr_3 QDs and is essential for improving the QY and stability. By changing the ligand from OA to a stronger binding ligand, such as 3-(*N,N*-dimethyloctadecylammonio)-propanesulfonate, there is no observable decrease in the PL intensity after 28 days in ambient air; previously, there was a 72% decrease (Fig. 16b–d) [97]. However, too strong binding can have an adverse effect by destroying the crystallinity of QDs.

When thiol is used as the ligand for CsPbBr_3 QDs, the PL intensity is decreased [119, 122]. The use of *L*-type ligands, such as tri-*n*-octylphosphine oxide or tetradecylphosphonic acid (TDPA), could possibly also improve the stability of CsPbBr_3 QDs [116, 120]. When tri-*n*-octylphosphine oxide was used, there was only a 5% decrease in PL intensity of CsPbBr_3 QDs in ethanol after 100 min [116]. With TDPA, a 15% decrease in the PL intensity was observed after 5 h in water, which was remarkable because a 93% decrease in the PL intensity was observed for the QDs without ligands. (Fig. 16a) [120] OA and OLA are the typical ligands used to make LFAlHP QDs; however, there are almost no reports on the use of different ligands. Previous works on CsPbBr_3 QD ligands indicate that selecting the appropriate one could possibly increase stability in LFAlHP QDs.

5.3 Possible application and materials in the future

The development of LFAlHP QDs has focused on materials with PL in visible region due to great interest in the application for LEDs, lasers, and photodetectors, and demonstrated their high potential to substitute conventional materials. They might also be a good alternative for plasmonic materials. Plasmonic materials are widely used to make transparent conducting oxides, smart windows, and nano-biomedicines,

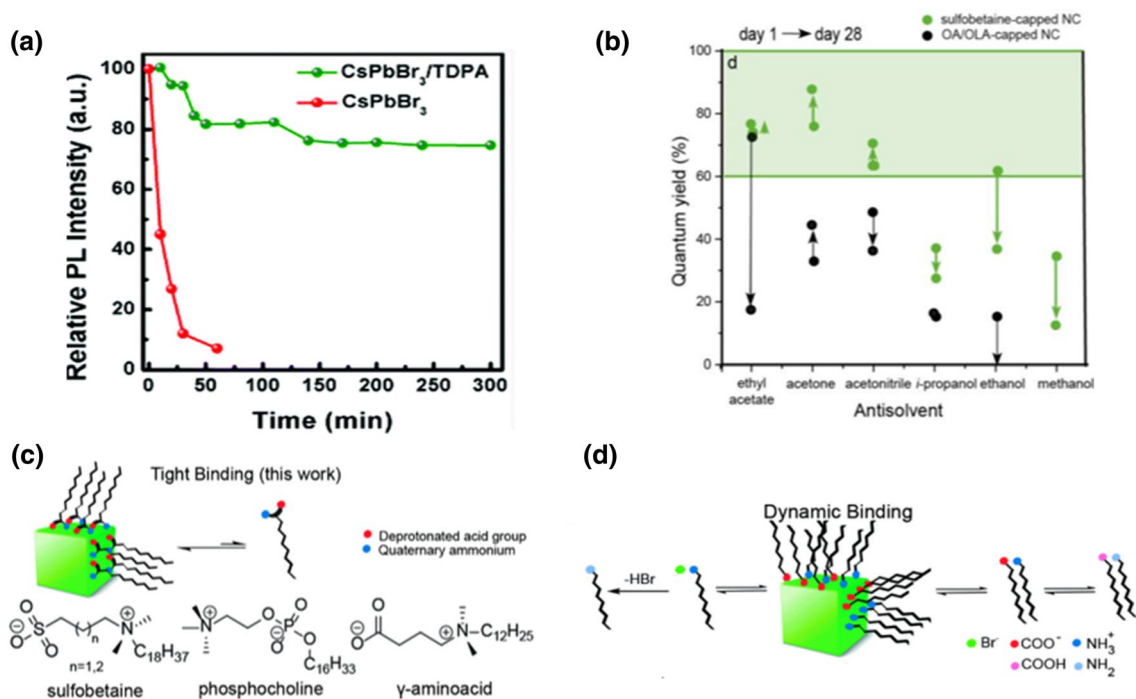


Fig. 16 **a** The relative PL intensity $\text{CsPbBr}_3/\text{TDPA}$ QDs and pure CsPbBr_3 QDs as a function of time in water. Adapted with permission from Ref. [120]. **b** QY of NCs covered with the 3-(*N,N*-dimethyloctadecylammonio)propanesulfonate and OA/OLA after two steps of purification on day 1 and after storage for 28 days. Adapted with

permission from Ref. [97]. **c** Depiction of conventional ligand capping of Perovskite NCs Using long-chain molecules with single head groups, in the ionized form (OA^- or Br^- , OLAH^+) and **d** a novel strategy wherein cationic and anionic groups are combined in a single zwitterionic molecule. Adapted with permission from Ref. [97]

which require the absorbance of localized surface plasmon resonance (LSPR) in the NIR region with high free-electron concentration. A localized surface plasmon resonance (LSPR) means the collective oscillation of free electrons and holes from absorbance of electromagnetic wave at the surface of nanomaterials. Aliovalently-doped oxide semiconductors, oxygen vacancy doped metal oxides, or self-doped copper chalcogenides had been the previous suggestions until recently [8]. Considering the wide variety of LFAIHPs and some materials with band gaps in the NIR region among them, the efficient LSPR can occur in nanoscale-sized materials. Thus, LFAIHP QDs could be a promising candidate. Therefore, we need to investigate new LFAIHPs and consider the methods, for example, Cu-based perovskites, used to synthesize them in QDs. In recent studies, $\text{Cs}_4\text{CuSb}_2\text{Cl}_{12}$, a $\langle 111 \rangle$ -oriented layered perovskite with a direct band gap of 1 eV, has been synthesized [108, 117, 121]. A high conductivity was observed showing a value more than 1 order greater compared with that of MAPbI_3 [108]. Moreover, the photo-, thermal-, and moisture-stability are good [108]. It is an intrinsic p-type semiconductor, which shows a high conductivity and high hole concentration under Cl-rich or Cd-poor atmosphere [121]. Although the material itself is quite new and further investigations are required to fully understand its properties and applications, in addition to requirement of new synthesizing method for making it into QDs, there is no doubt that it could prove to be a powerful candidate.

Relatively well-studied LFAIHP QDs, $\text{Cs}_3\text{Bi}_2\text{X}_9$ QDs can be further applied in scintillation to convert X-rays to UV or visible light. The process needs electron–hole pair generation using incoming radiation, creating a luminescent state. The photoexcited electron–hole pair is relaxed to the ground state from the generated luminescent state. Due to the high Z value of Cs, Bi, and I, $\text{Cs}_3\text{Bi}_2\text{I}_9$ QDs and $\text{Cs}_3\text{Bi}_2\text{Br}_9$ QDs can have a large attenuation coefficient meaning effective absorbance of X-rays or gamma-rays. There is possible application in the medical field, particularly, in radiotherapy. There is already a report that $\text{Cs}_3\text{Bi}_2\text{I}_9$ single crystal demonstrated excellent X-sensitivity. Sun et al. [123] reported that the X-ray sensitivity of the $\text{Cs}_3\text{Bi}_2\text{I}_9$ single crystal is $111.9 \mu\text{CGy}^{-1} \text{cm}^{-2}$. Doping luminescent lanthanide ions such as Ce^{3+} , Eu^{3+} , Tb^{3+} will make it possible to use $\text{Cs}_3\text{Bi}_2\text{X}_9$ QDs in polytherapy. For example, Gd-doped $\text{Cs}_3\text{Bi}_2\text{X}_9$ QDs can be used as multimodal imaging agents, and Ce- or Gd-doped $\text{Cs}_3\text{Bi}_2\text{X}_9$ QDs can be used as fluorescence agent in X-ray absorption.

In this article, we reviewed the current state of lead-free all-inorganic halide perovskite quantum dots. The search for new materials will widen the application scope of LFAIHP QDs, especially in the medical field, as the current use of Pb-based halide perovskites is not feasible owing to their toxicity. The compositional flexibility of halide perovskites

enables the synthesis of a wide variety of materials. More research on existing LFAIHP QDs should also be conducted. There are virtually no LFAIHP QDs that are entirely understood with respect to their optical and electrical properties. Moreover, for practical applications, their stability and QY should be improved, for which, doping, alloying, ligand control, and encapsulation might be particularly useful techniques.

Acknowledgements This research was financially supported by the Future Material Discovery Program. (NRF-2016M3D1A1027666).

References

1. X. Ren, H.S. Jung, Recent progress in flexible perovskite solar cell development. *J. Korean Ceram. Soc.* **55**(4), 325–336 (2018)
2. D. Liang, Y. Peng, Y. Fu, M.J. Shearer, J. Zhang, J. Zhai, Y. Zhang, R.J. Hamers, T.L. Andrew, S. Jin, Color-pure violet-light-emitting diodes based on layered lead halide perovskite nanoplates. *ACS Nano* **10**(7), 6897–6904 (2016)
3. H. Kim, J.S. Han, J. Choi, S.Y. Kim, H.W. Jang, Halide perovskites for applications beyond photovoltaics. *Small Methods* **2**(3), 1700310 (2018)
4. H. Kim, J.S. Han, S.G. Kim, S.Y. Kim, H.W. Jang, Halide perovskites for resistive random-access memories. *J. Mater. Chem. C* **7**(18), 5226–5234 (2019)
5. S.G. Kim, J.S. Han, H. Kim, S.Y. Kim, H.W. Jang, Recent advances in memristive materials for artificial synapses. *Adv. Mater. Technol.* **3**(12), 1800457 (2018)
6. J. Choi, S. Park, J. Lee, K. Hong, D.-H. Kim, C.W. Moon, G.D. Park, J. Suh, J. Hwang, S.Y. Kim, H.S. Jung, N.-G. Park, S. Han, K.T. Nam, H.W. Jang, Organolead halide perovskites for low operating voltage multilevel resistive switching. *Adv. Mater.* **28**(31), 6562–6567 (2016)
7. J. Lu, X. Sheng, G. Tong, Z. Yu, X. Sun, L. Yu, X. Xu, J. Wang, J. Xu, Y. Shi, K. Chen, Ultrafast solar-blind ultraviolet detection by inorganic perovskite CsPbX_3 quantum dots radial junction architecture. *Adv. Mater.* **29**(23), 1700400 (2017)
8. S. Ghosh, B. Pradhan, Lead-free metal halide perovskite nanocrystals: challenges, applications, and future aspects. *Chem. Nano Mat.* **5**(3), 300–312 (2019)
9. J. Choi, J.S. Han, K. Hong, S.Y. Kim, H.W. Jang, Organic-inorganic hybrid halide perovskites for memories, transistors, and artificial synapses. *Adv. Mater.* **30**(42), 1704002 (2018)
10. Y. Dong, D. Parobek, D.H. Son, Controlling quantum confinement and magnetic doping of cesium lead halide perovskite nanocrystals. *J. Korean Ceram. Soc.* **55**(6), 515–526 (2018)
11. S.M. Lee, J. Choi, J.B. Jeon, B.J. Kim, J.S. Han, T.L. Kim, H.S. Jung, H.W. Jang, Conducting bridge resistive switching behaviors in cubic MAPbI_3 , orthorhombic RbPbI_3 , and their mixtures. *Adv. Electron. Mater.* **5**(2), 1800586 (2019)
12. J. Choi, Q.V. Le, K. Hong, C.W. Moon, J.S. Han, K.C. Kwon, P.-R. Cha, Y. Kwon, S.Y. Kim, H.W. Jang, Enhanced endurance organolead halide perovskite resistive switching memories operable under an extremely low bending radius. *ACS Appl. Mater. Interfaces* **9**(36), 30764–30771 (2017)
13. J.S. Han, Q.V. Le, J. Choi, H. Kim, S.G. Kim, K. Hong, C.W. Moon, T.L. Kim, S.Y. Kim, H.W. Jang, Lead-free all-inorganic cesium tin iodide perovskite for filamentary and interface-type resistive switching toward environment-friendly and temperature-tolerant nonvolatile memories. *ACS Appl. Mater. Interfaces* **11**(8), 8155–8163 (2019)

14. W. Xiang, W. Tress, Review on recent progress of all-inorganic metal halide perovskites and solar cells. *Adv. Mater.* **31**(44), 1902851 (2019)
15. M.A.A. Wadi, T.H. Chowdhury, I.M. Bedja, J.-J. Lee, N. Amin, Md Aktharuzzaman, A. Islam, Evolution of Pb-free and partially Pb-substituted perovskite absorbers for efficient perovskite solar cells. *Electron. Mater. Lett.* **15**, 525–546 (2019). <https://doi.org/10.1007/s13391-019-00149-4>
16. Q.V. Le, K.T. Hong, H.W. Jang, S.Y. Kim, Halide perovskite quantum dots for light-emitting diodes: properties, synthesis, applications, and outlooks. *Adv. Electron. Mater.* **4**(12), 1800335 (2018)
17. S.E. Ju, J. Kim, Quantum dot light-emitting diodes employing phosphorescent organic molecules as double emission layers. *Electron. Mater. Lett.* **15**, 363–367 (2019)
18. Y. Wei, Z.Y. Cheng, J. Lin, An overview on enhancing the stability of lead halide perovskite quantum dots and their applications in phosphor-converted LEDs. *Chem. Soc. Rev.* **48**(1), 310–350 (2019)
19. S.S. Khanlfin, Y. Bekenstein, Advances in lead-free double perovskite nanocrystals, engineering band-gaps and enhancing stability through composition tunability. *Nanoscale* **11**(18), 8665–8679 (2019)
20. W. Lv, L. Li, M. Xu, J. Hong, X. Tang, L. Xu, Y. Wu, R. Zhu, R. Chen, W. Huang, Improving the stability of metal halide perovskite quantum dots by encapsulation. *Adv. Mater.* **31**(28), 1900682 (2019)
21. L. Zhou, Y.F. Xu, B.-X. Chen, D.-B. Kuang, C.-Y. Su, Synthesis and photocatalytic application of stable lead-free Cs₂AgBiBr₆ perovskite nanocrystals. *Small* **14**(11), 1703762 (2018)
22. Y. Bekenstein, J.C. Dahl, J. Huang, W.T. Osowiecki, J.K. Swabeck, E.M. Chan, P.D. Yang, A.P. Alivisatos, The making and breaking of lead-free double perovskite nanocrystals of cesium silver–bismuth halide compositions. *Nano Lett.* **18**(6), 3502–3508 (2018)
23. T.C. Jellicoe, J.M. Richter, H.F.J. Glass, M. Tabachnyk, R. Brady, S.E. Dutton, A. Rao, R.H. Friend, D. Credgington, N.C. Greenham, M.L. Bohm, Synthesis and optical properties of lead-free cesium tin halide perovskite nanocrystals. *J. Am. Chem. Soc.* **138**(9), 2941–2944 (2016)
24. L. Protesescu, S. Yakunin, O. Nazarenko, D.N. Dirin, M.V. Kovalenko, Low-cost synthesis of highly luminescent colloidal lead halide perovskite nanocrystals by wet ball milling. *ACS Appl. Nano Mater.* **1**(3), 1300–1308 (2018)
25. D.N. Dirin, L. Protesescu, D. Trummer, I.V. Kochetygov, S. Yakunin, F. Krumeich, N.P. Stadie, M.V. Kovalenko, Harnessing defect-tolerance at the nanoscale: highly luminescent lead halide perovskite nanocrystals in mesoporous silica matrixes. *Nano Lett.* **16**(9), 5866–5894 (2016)
26. A. Kojima, M. Ikegami, K. Teshima, T. Miyasaka, Highly luminescent lead bromide perovskite nanoparticles synthesized with porous alumina media. *Chem. Lett.* **41**(4), 397–399 (2012)
27. Y. Tong, E. Bladt, M. F. Ayc'uler, A. Manzi, K. Milowska, V. A. Hintermayr, P. Docampo, S. Bals, A. Urban, P. Lakshminarayana and J. Feldmann, Highly Luminescent Cesium Lead Halide Perovskite Nanocrystals with Tunable Composition and Thickness by Ultrasonication, *Angew. Chem. Int. Ed.* **55**(44), 13887–13892 (2016)
28. D.M. Jang, D.H. Kim, K. Park, J. Park, J.W. Lee, J.K. Song, Ultrasound synthesis of lead halide perovskite nanocrystals. *J. Mater. Chem. C* **4**(45), 10625–10629 (2016)
29. Y. Tong, B.J. Bohn, E. Bladt, K. Wang, P. Muller-Buschbaum, S. Bals, A.S. Urban, L. Polavarapu, J. Feldmann, From precursor powders to CsPbX₃ perovskite nanowires: one-pot synthesis, growth mechanism, and oriented self-assembly. *Angew. Chem. Int. Ed.* **56**(44), 13887–13892 (2017)
30. H. Huang, Q. Xue, B. Chen, Y. Xiong, J. Schneider, C. Zhi, H. Zhong, A.L. Rogach, Top-down fabrication of stable methylammonium lead halide perovskite nanocrystals by employing a mixture of ligands as coordinating solvents. *Angew. Chem. Int. Ed. Engl.* **129**(32), 9699–9704 (2017)
31. J. Shamsi, A.S. Urban, M. Imran, L.D. Trizio, L. Manna, Metal halide perovskite nanocrystals: synthesis, post-synthesis modifications, and their optical properties. *Chem. Rev.* **119**(5), 3296–3348 (2019)
32. S. Ghosh, S. Paul, and S. Kumar De, Control Synthesis of Air-Stable Morphology Tunable Pb-Free Cs₂SnI₆ Perovskite Nanoparticles and Their Photodetection Properties, *Part. Part. Syst. Charact.* **35**(9), 1800199 (2018)
33. Y. Xu, S. Li, Z. Zhang, Y. Hu, L. Yuan, W. Chen, Z.H. Chen, R. Patterson, S.J. Huang, Ligand-mediated synthesis of colloidal Cs₂SnI₆ three-dimensional nanocrystals and two-dimensional nanoplatelets. *Nanotechnology* **30**(29), 295601 (2019)
34. A. Wang, X. Yan, M. Zhang, S. Sun, M. Yang, W. Shen, X. Pan, P. Wang, Z. Deng, Controlled synthesis of lead-free and stable perovskite derivative Cs₂SnI₆ nanocrystals via a facile hot-injection process. *Chem. Mater.* **28**(22), 8132–8140 (2016)
35. D.S. Dolzhenkov, C. Wang, Y. Xu, M.G. Kanatzidis, E.A. Weiss, Ligand-free, quantum-confined Cs₂SnI₆ perovskite nanocrystals. *Chem. Mater.* **29**(18), 7901–7907 (2017)
36. E. Yassitepe, Z.Y. Yang, O. Voznyy, Y.H. Kim, G. Walters, J.A. Castañeda, P. Kanjanaboos, M. Yuan, X. Gong, F. Fan, J. Pan, S. Hoogland, R. Comin, O.M. Bakr, L.A. Padilha, A.F. Nogueira, E.H. Sargent, Amine-free synthesis of cesium lead halide perovskite quantum dots for efficient light-emitting diodes. *Adv. Funct. Mater.* **26**(47), 8757–8763 (2016)
37. S.E. Creutz, E.N. Crites, M.C.D. Siena, D.R. Gamelin, Colloidal nanocrystals of lead-free double-perovskite (elpasolite) semiconductors: synthesis and anion exchange to access new materials. *Nano Lett.* **18**(2), 1118–1123 (2018)
38. K. Hong, Q.V. Le, S.Y. Kim, H.W. Jang, Low-dimensional halide perovskites: review and issues. *J. Mater. Chem. C* **6**(9), 2189–2209 (2018)
39. J.V. Embden, A.S.R. Chesman, J.J. Jasieniak, The heat-up synthesis of colloidal nanocrystals. *Chem. Mater.* **27**(7), 2246–2285 (2015)
40. S. Wei, Y.C. Yang, X.J. Kang, L. Wang, L.J. Huang, D.C. Pan, Room-temperature and gram-scale synthesis of CsPbX₃ (X = Cl, Br, I) perovskite nanocrystals with 50–85% photoluminescence quantum yields. *Chem. Commun.* **52**(45), 7265–7268 (2016)
41. M. Leng, Y. Yang, K. Zeng, Z. Chen, Z. F. Tan, S. Li, J. Li, B. Xu, D. B. Li, M. P. Hautzinger, YP. Fu, T. Zhai, L. Xu, G. D. Niu, S. Jin and J. Tang, All-inorganic bismuth-based perovskite quantum dots with bright blue photoluminescence and excellent stability, *Adv. Funct. Mater.* **28**(1), 1704446 (2018)
42. J. Zhang, Y. Yang, H. Deng, U. Farooq, X.K. Yang, J. Khan, J. Tang, H. Song, High quantum yield blue emission from lead-free inorganic antimony halide perovskite colloidal quantum dots. *ACS Nano* **11**(9), 9294–9302 (2017)
43. B. Yang, J.S. Chen, F. Hong, X. Mao, K. Zheng, S.Q. Yang, Y. Li, T. Pullerits, W. Deng, K. Han, Lead-free, air-stable all-inorganic cesium bismuth halide perovskite nanocrystals. *Angew. Chem. Int. Ed.* **56**(41), 12471–12475 (2017)
44. P. Yang, G. Liu, B. Liu, X. Liu, Y. Lou, J. Chen, Y. Zhao, All-inorganic Cs₂CuX₄ (X = Cl, Br, and Br/I) perovskite quantum dots with blue-green luminescence. *Chem. Commun.* **54**(82), 11638–11641 (2018)
45. I. Lignos, S. Stavrakis, G. Nedelcu, L. Protesescu, A.J. Mello, M.V. Kovalenko, Synthesis of cesium lead halide perovskite nanocrystals in a droplet-based microfluidic platform: fast parametric space mapping. *Nano Lett.* **16**(3), 1869–1877 (2016)

46. F. Zhang, H. Zhong, C. Chen, X.-G. Wu, X. Hu, H. Huang, J. Han, B. Zou, Y. Dong, Brightly luminescent and color-tunable colloidal $\text{CH}_3\text{NH}_3\text{PbX}_3$ ($X = \text{Br}, \text{I}, \text{Cl}$) quantum dots: potential alternatives for display technology. *ACS Nano* **9**(4), 4533–4542 (2015)
47. F. Zhang, S. Huang, P. Wang, X. Chen, S. Zhao, Y. Dong, H. Zhong, Colloidal synthesis of air-stable $\text{CH}_3\text{NH}_3\text{PbI}_3$ quantum dots by gaining chemical insight into the solvent effects. *Chem. Mater.* **29**(8), 3793–3799 (2017)
48. H. Huang, F. Zhao, L. Liu, F. Zhang, X.-G. Wu, L. Shi, B. Zou, Q. Pei, H. Zhong, Emulsion synthesis of size-tunable $\text{CH}_3\text{NH}_3\text{PbBr}_3$ quantum dots: an alternative route toward efficient light-emitting diodes. *ACS Appl. Mater. Interfaces* **7**(51), 28128–28133 (2015)
49. M.A. Malik, M.Y. Wani, M.A. Hashim, Microemulsion method: a novel route to synthesize organic and inorganic nanomaterials. *Arab. J. Chem.* **5**(4), 397–417 (2012)
50. J.N. Lalena, D.A. Cleary, E.E. Carpenter, and N.F. Dean, Inorganic materials synthesis and fabrication. (Wiley, 2007), pp. 211–231
51. S.B. Sun, D. Yuan, Y. Xu, A. Wang, Z. Deng, Ligand-mediated synthesis of shape-controlled cesium lead halide perovskite nanocrystals via reprecipitation process at room temperature. *ACS Nano* **10**(3), 3648–3657 (2016)
52. R.F. Ali, I. Andreu, B.D. Gates, Green solvent assisted synthesis of cesium bismuth halide perovskite nanocrystals and the influences of slow and fast anion exchange rates. *Nanoscale Adv.* **1**(11), 4442–4449 (2019)
53. J.S. Bechtel, A. Van der Ven, Octahedral tilting instabilities in inorganic halide perovskites. *Phys. Rev. Mater.* **2**(2), 025401 (2018)
54. R.X. Yang, J.M. Skelton, E.L.D. Silva, J.M. Frost, A. Walsh, Spontaneous octahedral tilting in the cubic inorganic cesium halide perovskites CsSnX_3 and CsPbX_3 ($X = \text{F}, \text{Cl}, \text{Br}, \text{I}$). *J. Phys. Chem. Lett.* **8**(19), 4720–4726 (2017)
55. F. Deschler, M. Price, S. Pathak, L. E. Klintberg, D. -D. Jarausch, R. Higler, S. Hüttner, T. Leijtens, S. D. Stranks, H. J. Snaith, M. Atature, R. T. Phillips, and R. H. Friend, High photoluminescence efficiency and optically pumped lasing in solution-processed mixed halide perovskite semiconductors, *J. Phys. Chem. Lett.* **5**(8), 1421–1426 (2014)
56. Chung, J.-H. Song, J. Im, J. Androulakis, C. D. Malliakas, H. Li, A. J. Freeman, J. T. Kenney, and M. G. Kanatzidis, CsSnI_3 : Semiconductor or metal? High electrical conductivity and strong near-infrared photoluminescence from a single material. high hole mobility and phase-transitions, *J. Am. Chem. Soc.* **134**(20), 8579–8587 (2012)
57. J.J. Luo, M.C. Hu, G.D. Niu, J.A. Tang, Lead-free halide perovskites and perovskite variants as phosphors toward light-emitting applications. *ACS Appl. Mater. Interfaces* **11**(35), 31575–31584 (2019)
58. W.M. Timmermans, S.O. Cholakh, G. Blasse, The luminescence of $\text{Cs}_3\text{Bi}_2\text{Cl}_9$ and $\text{Cs}_3\text{Sb}_2\text{Cl}_9$. *J. Solid State Chem.* **46**(2), 222–233 (1983)
59. W.M. Timmermans, G. Blasse, The luminescence and photoconductivity of $\text{Cs}_3\text{Bi}_2\text{Br}_9$ single crystals. *J. Lumin.* **24–25**(1), 75–78 (1981)
60. K.M. McCall, C.C. Stoumpos, S.S. Kostina, M.G. Kanatzidis, B.W. Wessels, Strong electron–phonon coupling and self-trapped excitons in the defect halide perovskites $\text{A}_3\text{M}_2\text{I}_9$ ($A = \text{Cs}, \text{Rb}; M = \text{Bi}, \text{Sb}$). *Chem. Mater.* **29**(9), 4129–4145 (2017)
61. Wang, Y. Guo, Z. Zhou, X. Niu, Y. Wang, F. Muhammad, H. Li, T. Zhang, J. Wang, S. Nie, and Z. Deng, Aqueous acid-based synthesis of lead-free tin halide perovskites with near-unity photoluminescence quantum efficiency, *Chem. Sci.* **10**(17), 4573–4579 (2019)
62. V. Kovalenko, L. Manna, A. Cabot, Z. Hens, D.V. Talapin, C.R. Kagan, V.I. Klimov, A.L. Rogach, P. Reiss, D.J. Milliron, P. Guyot-Sionnest, G. Konstantatos, W.J. Parak, T. Hyeon, B.A. Korgel, C.B. Murray, W. Heiss, Prospects of nanoscience with nanocrystals. *ACS Nano* **9**(2), 1012–1057 (2015)
63. M.A. Boles, D. Ling, T. Hyeon, D.V. Talapin, The surface science of nanocrystals. *Nat. Mater.* **15**, 141–153 (2016)
64. Y. Lou, M. Fang, J.X. Chen, Y.X. Zhao, Formation of highly luminescent cesium bismuth halide perovskite quantum dots tuned by anion exchange. *Chem. Commun.* **54**(30), 3779–3782 (2018)
65. J. Pal, A. Bhunia, S.D. Chakraborty, S. Manna, S. Das, A. Dewan, S. Datta, A. Nag, Synthesis and optical properties of colloidal $\text{M}_3\text{Bi}_2\text{I}_9$ ($M = \text{Cs}, \text{Rb}$) perovskite nanocrystals. *J. Phys. Chem. C* **122**(19), 10643–10649 (2018)
66. F. Jiang, D. Yang, Y. Jiang, T. Liu, X. Zhao, Y. Ming, B. Luo, F. Qin, J. Fan, H. Han, L. Zhang, Y. Zhou, Chlorine-incorporation-induced formation of the layered phase for antimony-based lead-free perovskite solar cells. *J. Am. Chem. Soc.* **140**(3), 1019–1027 (2018)
67. E.P. Booker, J.T. Griffiths, L. Eyre, C. Ducati, N.C. Greenham, N.J.L.K. Davis, Synthesis, characterization, and morphological control of Cs_2CuCl_4 nanocrystals. *J. Phys. Chem. C* **123**(27), 16951–16956 (2019)
68. M. Zhang, H. Yu, M. Lyu, Q. Wang, J.H. Yun, L. Wang, Composition-dependent photoluminescence intensity and prolonged recombination lifetime of perovskite $\text{CH}_3\text{NH}_3\text{PbBr}_{(3-x)}\text{Cl}_x$ films. *Chem. Commun.* **50**(79), 11727–11730 (2014)
69. C. Brink, N.F. Binnendijk, J.V.D. Linde, The crystal structures of CsCu_2Cl_3 and CsAg_2I_3 . *Acta. Crystallogr.* **7**(2), 176–180 (1954)
70. V. Kumar Ravi, N. Singhal, and A. Nag, Initiation and future prospects of colloidal metal halide double-perovskite nanocrystals: $\text{Cs}_2\text{AgBiX}_6$ ($X = \text{Cl}, \text{Br}, \text{I}$), *J. Mater. Chem. A* **6**(44), 21666–21675 (2018)
71. H. Slavney, T. Hu, A.M. Lindenberg, H.I. Karunadasa, A bismuth-halide double perovskite with long carrier recombination lifetime for photovoltaic applications. *J. Am. Chem. Soc.* **138**(7), 2138–2141 (2016)
72. F. Locardi, M. Cirignano, D. Baranov, Z. Dang, M. Prato, F. Drago, M. Ferretti, V. Pinchetti, M. Fanciulli, S. Brovelli, L. De Trizio, L. Manna, Colloidal synthesis of double perovskite $\text{Cs}_2\text{AgInCl}_6$ and Mn-doped $\text{Cs}_2\text{AgInCl}_6$ nanocrystals. *J. Am. Chem. Soc.* **140**(40), 12989–12995 (2018)
73. B. Yang, J. Chen, S. Yang, F. Hong, L. Sun, P. Han, T. Pullerits, W. Deng, K. Han, Lead-free silver-bismuth halide double perovskite nanocrystals. *Angew. Chem. Int. Ed.* **57**(19), 5359–5363 (2018)
74. E. M. Sanehira, A. R. Marshall, J. A. Christians, S. P. Harvey, P. N. Ciesielski, L. M. Wheeler, P. Schulz, L. Y. Lin, M. C. Beard, and J. M. Luther, Enhanced mobility CsPbI_3 quantum dot arrays for record-efficiency, high-voltage photovoltaic cells, *Sci. Adv.* **3**(10), eaao4204 (2017)
75. A. Swarnkar, A.R. Marshall, E.M. Sanehira, B.D. Chernomordik, D.T. Moore, J.A. Christians, T. Chakrabarti, J.M. Luther, Quantum dot–induced phase stabilization of α - CsPbI_3 perovskite for high-efficiency photovoltaics. *Science* **354**(6308), 92–95 (2016)
76. F. Liu, C. Ding, Y. Zhang, T.S. Ripolles, T. Kamisaka, T. Toyoda, S. Hayase, T. Minemoto, K. Yoshino, S. Dai, M. Yanagida, H. Noguchi, Q. Shen, Colloidal synthesis of air-stable alloyed $\text{CsSn}_{1-x}\text{Pb}_x\text{I}_3$ perovskite nanocrystals for use in solar cells. *J. Am. Chem. Soc.* **139**(46), 16708–16719 (2017)
77. K.P. Marshall, R.I. Walton, R.A. Hutton, Tin perovskite/fullerene planar layer photovoltaics: improving the efficiency and stability of lead-free devices. *J. Mater. Chem. A* **3**(21), 11631–11640 (2015)

78. M. Chen, M.G. Ju, H.F. Garces, A.D. Carl, L.K. Ono, Z. Hawash, Y. Zhang, T. Shen, Y. Qi, R.L. Grimm, D. Pacifici, X.C. Zeng, Y. Zhou, N.P. Padture, Highly stable and efficient all-inorganic lead-free perovskite solar cells with native-oxide passivation. *Nat. Commun.* **10**, 16 (2019)
79. F. Giustino, H.J. Snaith, Toward lead-free perovskite solar cells. *ACS Energy Lett.* **1**(6), 1233–1240 (2016)
80. M. -G. Ju, M. Chen, Y. Zhou, H. F. Garces, J. Dai, L. Ma, N. P. Padture, and X. C. Zeng, earth-abundant nontoxic titanium(IV)-based vacancy-ordered double perovskite halides with tunable 1.0 to 1.8 eV bandgaps for photovoltaic applications, *ACS Energy Lett.* **3**(2), 297–304 (2018)
81. X. Qiu, Y. Jiang, H. Zhang, Z. Qiu, S. Yuan, P. Wang, B. Cao, Lead-free mesoscopic Cs₂SnI₆ perovskite solar cells using different nanostructured ZnO nanorods as electron transport layers. *Phys. Status Solidi RRL* **10**(8), 587–591 (2016)
82. X. Qiu, B. Cao, S. Yuan, X. Chen, Z. Qiu, Y. Jiang, Q. Ye, H. Wang, H. Zeng, J. Liu, and M. G. Kanatzidis, From unstable CsSnI₃ to air-stable Cs₂SnI₆: A lead-free perovskite solar cell light absorber with bandgap of 1.48 eV and high absorption coefficient, *Sol. Energy Mater. Sol. Cells* **159**, 227–234 (2017)
83. M. Chen, M.-G. Ju, A.D. Carl, Y. Zong, R.L. Grimm, J. Gu, X.C. Zeng, Y. Zhou, N.P. Padture, Cesium titanium(IV) bromide thin films based stable lead-free perovskite solar cells. *Joule* **2**(3), 558–570 (2018)
84. E. Greul, M.L. Petrus, A. Binek, P. Docampo, T. Bein, Highly stable, phase pure Cs₂AgBiBr₆ double perovskite thin films for optoelectronic applications. *J. Mater. Chem. A* **5**(37), 19972–19981 (2017)
85. Q. Zhang, Y. Yin, All-inorganic metal halide perovskite nanocrystals: opportunities and challenges. *ACS Cent. Sci.* **4**(6), 668–679 (2018)
86. R.L.Z. Hoye, L. Eyre, F. Wei, F. Brivio, A. Sadhanala, S. Sun, W. Li, K.H.L. Zhang, J.L. MacManus-Driscoll, P.D. Bristowe, R.H. Friend, A.K. Cheetham, F. Deschler, Fundamental carrier lifetime exceeding 1 μs in Cs₂AgBiBr₆ double perovskite. *Adv. Mater. Interfaces* **5**(15), 1800464 (2018)
87. C.C. Wu, Q.H. Zhang, Y. Liu, W. Luo, X. Guo, Z.R. Huang, H. Ting, W.H. Sun, S.Y. Wei, S.F. Wang, Z.J. Chen, L.X. Xiao, The dawn of lead-free perovskite solar cell: highly stable double perovskite Cs₂AgBiBr₆ film. *Adv. Sci. (Weinh)* **5**(3), 1700759 (2018)
88. D. Liang, Y.L. Peng, Y.P. Fu, M.J. Shearer, J.J. Zhang, J.Y. Zhai, Y. Zhang, R.J. Hamers, T.L. Andrew, S. Jin, High-performance CsPbX₃ perovskite quantum-dot light-emitting devices via solid-state ligand exchange. *ACS Appl. Nano Mater.* **1**(2), 488–496 (2018)
89. H.C. Cho, S.-H. Jeong, M.H. Park, Y.H. Kim, C. Wolf, C.-L. Lee, J.H. Heo, A. Sadhanala, N.S. Myoung, S. Yoo, S.H. Im, R.H. Friend, T.-W. Lee, Overcoming the electroluminescence efficiency limitations of perovskite light-emitting diodes. *Science* **350**(6265), 1222–1225 (2015)
90. Z.-K. Tan, R.S. Moghaddam, M.L. Lai, P. Docampo, R. Higler, F. Deschler, M. Price, A. Sadhanala, L.M. Pazos, D. Credgington, F. Hanusch, T. Bein, H.J. Snaith, R.H. Friend, Bright light-emitting diodes based on organometal halide perovskite. *Nat. Nanotech.* **9**(9), 687–692 (2014)
91. L.C. Schmidt, A. Pertegas, S. Gonzalez-Carrero, O. Malinkiewicz, S. Agouram, G.M. Espallargas, H.J. Bolink, R.E. Galian, J. Perez-Prieto, Nontemplate synthesis of CH₃NH₃PbBr₃ perovskite nanoparticles. *J. Am. Chem. Soc.* **136**(3), 850–853 (2014)
92. S. Gonzalez-Carrero, R.E. Galian, J. Pérez-Prieto, Maximizing the emissive properties of CH₃NH₃PbBr₃ perovskite nanoparticles. *J. Mater. Chem. A* **3**(17), 9187–9193 (2015)
93. B. Pradhan, G.S. Kumar, S. Sain, A. Dalui, U.K. Ghorai, S.K. Pradhan, S. Acharya, Size tunable cesium antimony chloride perovskite nanowires and nanorods. *Chem. Mater.* **30**(6), 2135–2142 (2018)
94. H. Huang, A.S. Sussha, S.V. Kershaw, T.F. Hung, A.L. Rogach, Control of emission color of high quantum yield CH₃NH₃PbBr₃ perovskite quantum dots by precipitation temperature. *Adv. Sci. (Weinh)* **2**(9), 1500194 (2015)
95. H.S. Moon, C.M. Lee, W.S. Lee, J.W. Kim, H.Y. Chae, Stability of quantum dots, quantum dot films, and quantum dot light-emitting diodes for display applications. *Adv. Mater.* **31**(34), 1804294 (2019)
96. H. Sun, Z. Yang, M. Wei, W. Sun, X. Li, S. Ye, Y. Zhao, H. Tan, E.L. Kynaston, T.B. Schon, H. Yan, Z. Lu, G. Ozin, E.H. Sargent, D.S. Seferos, Chemically addressable perovskite nanocrystals for light-emitting applications. *Adv. Mater.* **29**(34), 1701153 (2017)
97. F. Krieg, S. T. Ochsenein, S. Yakunin, S. ten Brinck, P. Aellen, A. Suess, B. Clerc, D. Guggisberg, O. Nazarenko, Y. Shynkarenko, S. Kumar, C. J. Shih, I. Infante, and M. V. Kovalenko, Colloidal CsPbX₃ (X = Cl, Br, I) Nanocrystals 2.0: zwitterionic capping ligands for improved durability and stability, *ACS Energy Lett.* **3**(3), 641–646 (2018)
98. F. Liu, Y.H. Zhang, C. Ding, S. Kobayashi, T. Izuishi, N. Nakazawa, T. Toyoda, T. Ohta, S. Hayase, T. Minemoto, K. Yoshino, S.Y. Dai, Q. Shen, Highly luminescent phase-stable CsPbI₃ perovskite quantum dots achieving near 100% absolute photoluminescence quantum yield. *ACS Nano* **11**(10), 10373 (2017)
99. Z. Li, L. Kong, S. Huang, and L. Li, Highly luminescent and ultrastable CsPbBr₃ perovskite quantum dots incorporated into a silica/alumina monolith, *Angew. Chem., Int. Ed.* **56**(28), 8134–8138 (2017)
100. P. Wang, S. Liu, W. Luo, H. Fang, F. Gong, N. Guo, Z.-G. Chen, J. Zou, Y. Huang, X. Zhou, J. Wang, X. Chen, W. Lu, F. Xiu, W. Hu, Arrayed van der Waals broadband detectors for dual-band detection. *Adv. Mater.* **29**(16), 1604439 (2017)
101. Y. Li, Z.-F. Shi, X.-J. Li, C.-X. Shan, Photodetectors based on inorganic halide perovskites: materials and devices. *Chin. Phys. B* **28**(1), 017803 (2019)
102. L.-Z. Lei, Z.F. Shi, Y. Li, Z.Z. Ma, F. Zhang, T.-T. Xu, Y.-T. Tian, D. Wu, X.-J. Lia, G.-T. Du, High-efficiency and air-stable photodetectors based on lead-free double perovskite Cs₂AgBiBr₆ thin films. *J. Mater. Chem. C* **6**(30), 7982–7988 (2018)
103. C. Wu, B. Du, W. Luo, Y. Liu, T. Li, D. Wang, X. Guo, H. Ting, Z. Fang, S. Wang, Z. Chen, Y. Chen, L. Xiao, Highly efficient and stable self-powered ultraviolet and deep-blue photodetector based on Cs₂AgBiBr₆/SnO₂ heterojunction. *Adv. Opt. Mater.* **6**(22), 1800811 (2018)
104. Y.-F. Xu, M.-Z. Yang, B.-X. Chen, X.-D. Wang, H.-Y. Chen, D.-B. Kuang, C.Y. Su, A CsPbBr₃ perovskite quantum dot/graphene oxide composite for photocatalytic CO₂ reduction. *J. Am. Chem. Soc.* **139**(16), 5660–5663 (2017)
105. Y. Wang, Z. Lv, Q. Liao, H. Shan, J. Chen, Y. Zhou, L. Zhou, X. Chen, V. A. L. Roy, Z. Wang, Z. Xu, Y. -J. Zeng, and S. -T. Han, Synergies of electrochemical metallization and valence change in all-inorganic perovskite quantum dots for resistive switching, *Adv. Mater.* **30**(28), 1800327(2018)
106. J.S. Han, Q.V. Le, J. Choi, K. Hong, C.W. Moon, T.L. Kim, H. Kim, S.Y. Kim, H.W. Jang, Air-stable cesium lead iodide perovskite for ultra-low operating voltage resistive switching. *Adv. Fuct. Mater.* **28**(5), 1705783 (2018)
107. S.G. Kim, Q.V. Le, J.S. Han, H. Kim, M.-J. Choi, S.A. Lee, T.L. Kim, S.B. Kim, S.Y. Kim, H.W. Jang, Dual-phase all-inorganic cesium halide perovskites for conducting-bridge memory-based artificial synapses. *Adv. Fuct. Mater.* **29**(49), 1906686 (2019)
108. B. Vargas, E. Ramos, E. Pérez-Gutiérrez, J.C. Alonso, D. Solís-Ibarra, A direct bandgap copper-antimony halide perovskite. *J. Am. Chem. Soc.* **139**(27), 9116–9119 (2017)

109. B. Yang, X. Mao, F. Hong, W. Meng, Y. Tang, X. Xia, S. Yang, W. Deng, K. Han, Lead-free direct band gap double-perovskite nanocrystals with bright dual-color emission. *J. Am. Chem. Soc.* **140**(49), 17001–17006 (2018)
110. K. Zheng, Q. Zhu, M. Abdellah, M.E. Messing, W. Zhang, A. Generalov, Y. Niu, L. Ribaud, S.E. Canton, T. Pullerits, Exciton binding energy and the nature of emissive states in organometal halide perovskites. *J. Phys. Chem. Lett.* **6**(15), 2969–2975 (2015)
111. Z. Liu, Y. Zhang, Y. Fan, Z. Chen, Z. Tang, J. Zhao, Y. Lv, J. Lin, X. Guo, J. Zhang, and X. Liu, Toward highly luminescent and stabilized silica-coated perovskite quantum dots through simply mixing and stirring under room temperature in air, *ACS Appl. Mater. Interfaces* **10**(15), 13053–13061 (2018)
112. M. Liu, A. Matuhina, H. Zhang, P. Vivo, Advances in the stability of halide perovskite nanocrystals. *Materials* **12**(22), 3733 (2019)
113. J. Morris-Cohen, M.D. Donakowski, K.E. Knowles, E.A. Weiss, The Effect of a common purification procedure on the chemical composition of the surfaces of CdSe quantum dots synthesized with trioctylphosphine oxide. *J. Phys. Chem. C* **114**(2), 897–906 (2010)
114. Q.A. Akkerman, G. Raino, M.V. Kovalenko, L. Manna, Genesis, challenges and opportunities for colloidal lead halide perovskite nanocrystals. *Nat. Mater.* **17**, 394–405 (2018)
115. M.H. Kumar, S. Dharani, W.L. Leong, P.P. Boix, R.R. Prabhakar, T. Baikie, C. Shi, H. Ding, R. Ramesh, M. Asta, M. Gratzel, S.G. Mhaisalkar, N. Mathews, Lead-free halide perovskite solar cells with high photocurrents realized through vacancy modulation. *Adv. Mater.* **26**(41), 7122–7127 (2014)
116. L.Z. Wu, Q.X. Zhong, D. Yang, M. Chen, H.C. Hu, Q. Pan, H.Y. Liu, M.H. Cao, Y. Xu, B.Q. Sun, Q. Zhang, Improving the stability and size tunability of cesium lead halide perovskite nanocrystals using trioctylphosphine oxide as the capping ligand. *Langmuir* **33**(44), 12689–12696 (2017)
117. N. Singhal, R. Chakraborty, P. Ghosh, A. Nag, Low-bandgap $\text{Cs}_4\text{CuSb}_2\text{Cl}_{12}$ layered double perovskite: synthesis, reversible thermal changes, and magnetic interaction. *Chem. Asian J.* **13**(16), 2085–2092 (2018)
118. X. Li, Y. Wu, S. Zhang, B. Cai, Y. Gu, J. Song, H. Zeng, CsPbX_3 Quantum dots for lighting and displays: room-temperature synthesis, photoluminescence superiorities, underlying origins and white light-emitting diodes. *Adv. Funct. Mater.* **26**(15), 2435–2445 (2016)
119. J. Kwak, W.K. Bae, M. Zorn, H. Woo, H. Yoon, J. Lim, S.W. Kang, S. Weber, H.J. Butt, R. Zentel, S. Lee, K. Char, C. Lee, Characterization of quantum dot/conducting polymer hybrid films and their application to light-emitting diodes. *Adv. Mater.* **21**(48), 5022 (2009)
120. T.T. Xuan, X.F. Yang, S.Q. Lou, J.J. Huang, Y. Liu, J.B. Yu, H.L. Li, K.L. Wong, C.X. Wang, J. Wang, Highly stable CsPbBr_3 quantum dots coated with alkyl phosphate for white light-emitting diodes. *Nanoscale* **9**(40), 15286–15290 (2017)
121. J. Xu, J.-B. Liu, J. Wang, B.-X. Liu, B. Huang, Prediction of novel p-type transparent conductors in layered double perovskites: a first-principles study. *Adv. Funct. Mater.* **28**(26), 1800332 (2018)
122. Z.K. Liu, Y. Bekenstein, X.C. Ye, S.C. Nguyen, J. Swabeck, D.D. Zhang, S.T. Lee, P.D. Yang, W.L. Ma, A.P. Alivisatos, Ligand mediated transformation of cesium lead bromide perovskite nanocrystals to lead depleted Cs_4PbBr_6 nanocrystals. *J. Am. Chem. Soc.* **139**(15), 5309–5312 (2017)
123. Q. Sun, Y. Xu, H. Zhang, B. Xiao, X. Liu, J. Dong, Y. Cheng, B. Zhang, W. Jie, M.G. Kanatzidis, Optical and electronic anisotropies in perovskitoid crystals of $\text{Cs}_3\text{Bi}_2\text{I}_9$ studies of nuclear radiation detection. *J. Mater. Chem. A* **6**(46), 23388–23395 (2018)
124. H. Bian, D. Bai, Z. Jin, K. Wang, L. Liang, H. Wang, J. Zhang, Q. Wang, and S. Liu, Graded bandgap $\text{CsPbI}_{2+x}\text{Br}_{1-x}$ perovskite solar cells with a stabilized efficiency of 14.4%, *Joule* **2**(8), 1500–1510 (2018)
125. T. Chiba, Y. Hayashi, H. Ebe, K. Hoshi, J. Sato, S. Sato, Y.-J. Pu, S. Ohisa, J. Kido, Anion-exchange red perovskite quantum dots with ammonium iodine salts for highly efficient light-emitting devices. *Nature Photon* **12**, 681–687 (2018)
126. J. Song, T. Fang, J. Li, L. Xu, F. Zhang, B. Han, Q. Shan, and H. Zeng, Organic–inorganic hybrid passivation enables perovskite QLEDs with an EQE of 16.48%, *Adv. Mater.* **30**(50), 1805409 (2018)

Publisher's Note Springer Nature remains neutral with regard to jurisdictional claims in published maps and institutional affiliations.